41st AIAA Fluid Dynamics Conference and Exhibit
27 - 30 June 2011, Honolulu, Hawaii

AIAA 2011-3249

Numerical Study of Hypersonic Flow Over an Isolated Roughness with a High-Order Cut-Cell Method

Patrick T. Greene*, Jeff D. Eldredge†, Xiaolin Zhong‡, and John Kim§
University of California, Los Angeles, CA, 90095-1597, USA

Results are presented for direct numerical simulations of hypersonic flow over an isolated roughness element located on a flat plate. The simulations were performed on a Cartesian grid with the roughness geometry imposed by a third-order cut-cell method. The simulations also utilize a fifth-order WENO scheme to capture any steep gradients in the flow created by the roughness. The combination results in a globally fourth-order scheme. Two-dimensional and three-dimensional test cases show very good agreement with results obtained from a body-fitted grid simulation. Preliminary results for Mach 6 flow over a $k/\delta = 0.75$ cylindrical roughness are reported. In addition, results from a series of simulations of Mach 6 flow over a three-dimensional Gaussian roughness performed with a body-fitted grid are presented.

I. Introduction

The ability to accurately predict the location of laminar to turbulent transition in boundary layers is of great importance to the design of hypersonic vehicles. At high Mach numbers, the viscous effects in the boundary layer can cause extreme surface temperatures as kinetic energy is transfer to thermal energy. When the flow transitions from laminar to turbulent, this heating is further increased by turbulent mixing near the wall. In addition to the thermal effects, turbulent flow also generates larger shear stresses which increase the friction drag on the surface. Without the knowledge of the transition location, designers of hypersonic vehicles must be overly cautious with their designs. Thermal protection and propulsion systems must assume turbulent flow over the entire body.[1] In spite of its importance, the mechanisms leading to the transition of hypersonic boundary layers are still poorly understood.[2] Predicting the location of transition is further complicated by the presence of surface roughness.

The effects of roughness elements have been documented for sometime experimentally. Schneider[2] has recently written a review of experiments studying the effect of roughness on hypersonic boundary-layer transition. Roughness elements generally cause the location of transition to move forward compared to flow without a roughness element. It is possible to have a small enough roughness element such that there is no effect on the transition location. Such a roughness is said to be below its critical height. Only a roughness element above this critical height will cause a change in the transition location. As the roughness height is increased past this critical height, the location of transition will continue to move closer to the roughness element. Eventually transition will occur at its closest location behind the roughness. This location may still be a finite distance downstream of the roughness. Further increases of the roughness height will no longer cause the transition location to move forward. The height at which this occurs is called the effective height. Although a great deal of research has been done to study the effects of roughness on hypersonic transition, most of the data was for correlations to be used in the design of hypersonic vehicles. Very little is actually known about the exact physics behind hypersonic boundary-layer transition with roughness elements.

In the recent past, a great deal of work went into exploring transient growth as an important role in roughness-induced transition. Tumin and Reshotko[3] presented a spatial theory for transient growth in boundary-layer flow. They showed that the most significant transient growth is associated with steady

*Graduate Student, Department of Mechanical and Aerospace Engineering, greene@seas.ucla.edu, AIAA Student Member.
†Associate Professor, Department of Mechanical and Aerospace Engineering, AIAA Member.
‡Professor, Department of Mechanical and Aerospace Engineering, AIAA Associate Fellow.
§Professor, Department of Mechanical and Aerospace Engineering, AIAA Member.

streamwise vortices. Roughness elements generate a horse-shoe vortex and a pair of vortices in their wake. This is exactly the kind of disturbance that Tumin and Reshotko showed would lead to optimal transient growth. White et al.[4,5,6] have performed a series of experiments involving subsonic flow over an array of cylindrical roughness elements and have identified transient growth in the wake of the array. Fischer and Choudhari[7] and Choudhari and Fischer[8] performed numerical simulations of White's experiments. They also confirmed the presence of transient growth. Reshotko and Tumin[9] used their spatial transient growth theory to produce a model for roughness-induced transition. Their model reproduced the trends of Reda and the passive nosetip technology (PANT) data.[10,11]

Recent work has shifted to the possible existence of an absolute instability being generated by the roughness. For taller roughness elements in subsonic flow, the wake region is dominated by unsteady hairpin vortices.[12] Ergin and White[13] conducted experiments of unsteady low-speed flow over isolated roughness elements. They found the locations of maximum fluctuation intensity to correspond to locations of inflection points in the streamwise velocity. This suggests that the unsteadiness seen in subsonic flow may have been caused by a Kelvin-Helmholtz type instability. The unsteady vortex shedding seen in subsonic flow is not present is supersonic flow.[14] This difference may be due to the stabilizing effect of high Mach numbers on shear layers.[15] Although the unsteadiness is no longer present, a similar instability may still remain. Danehy et al.[16] visualized Mach 4.2 flow over an isolated 2 mm radius hemispherical roughness element using Nitric oxide planar laser-induced fluorescence (PLIF). They showed that breakdown to turbulence begins in the downstream legs of the horse-shoe vortex that forms upstream of the roughness. Chang et al.[17] have recently performed numerical simulations that support these results. They found strong unsteadiness in Mach 4.16 flow over isolated cylindrical roughness elements with heights of 1.3 and 2.5 times the boundary-layer thickness with the unsteadiness first visible in the legs of the horse-shoe vortices. Spectral analysis and the computed evolution of disturbance root mean square amplitude suggest that the source for the unsteadiness is a possible absolute instability located in the separation region formed upstream of the roughness element. Bartkowicz et al.[18] have numerical simulated flow inside the Boeing/AFOSR Mach 6 quiet wind tunnel at Purdue University with a cylindrical roughness element and reproduced an instability which was measured experimentally.[19] They suggest that the instability is created by a high momentum jet created near the top of the roughness which flows down into the vortex system located near the wall.

The objective of the current paper is to study the physical mechanisms behind transition in hypersonic boundary layers due to isolated surface roughness. This will be accomplished by numerically simulating flow conditions similar to those of recent roughness experiments in the Boeing/AFOSR Mach 6 quiet wind tunnel at Purdue University.[19,20] The compressible Navier-Stokes equations are solved on a Cartesian grid using a fifth-order WENO scheme combined with a third-order cut-cell method to model the roughness. Two-dimensional and three-dimensional test cases for the cut-cell method will be presented. The two-dimensional results will be compared to results computed using a body-fitted grid and a continuous forcing immersed boundary method. Mach 6 flow over a three-dimensional Gaussian roughness computed with a body-fitted grid will also be presented. In addition, preliminary results of Mach 6 flow over a cylindrical roughness computed with the cut-cell method are reported.

II. Problem Statement

The geometry of interest is the Boeing/AFOSR Mach 6 quiet wind tunnel at Purdue University. The wind tunnel is a Ludwieg tube capable of generating quiet Mach 6 flow and is maintained by Professor Steven Schneider.[21] Wheaton and Schneider[19] have recently measured a 21 kHz instability in Pitot probe and hot-wire measurements for Mach 6 flow over a cylindrical roughness element with a height of 10.2 mm and a diameter of 5.97 mm. The undisturbed boundary layer had a thickness of approximately 9.23 mm. Ward et al.[20] measured the same instability with flush-mounted pressure transducers on the nozzle wall. The goal of the current study to reproduce these results and to investigate the source of the instability.

Initial numerical simulations were performed with a body-fitted grid and a Gaussian roughness. Due to difficulties in generating smooth grids with the roughness in the wind tunnel, the tunnel geometry was modeled as a flat plate. Although the geometry has changed, the same flow conditions as the Purdue wind tunnel have been used. Numerical simulation using a Gaussian roughness have been completed and simulations with a cylindrical roughness are currently underway.

III. Methodology

The governing equations in Cartesian coordinates, $(x_1, x_2, x_3) = (x, y, z)$, are the three-dimensional unsteady compressible Navier-Stokes equations for a calorically perfect gas with density ρ, pressure p, temperature T, and velocity $(u_1, u_2, u_3) = (u, v, w)$:

$$\frac{\partial \hat{\mathbf{U}}}{\partial t} + \frac{\partial \hat{\mathbf{F}}_j}{\partial x_j} = \frac{\partial \hat{\mathbf{F}}_{v,j}}{\partial x_j}, \quad j = 1, 2, 3 \tag{1}$$

where $\hat{\mathbf{U}}$ is the vector of conservative variables, $[\rho, \rho u, \rho v, \rho w, E]^T$. $\hat{\mathbf{F}}_j$ and $\hat{\mathbf{F}}_{v,j}$ are the vectors of the inviscid and viscous fluxes, respectively, in the jth direction and are given as

$$\hat{\mathbf{F}}_j = \begin{pmatrix} \rho u_j \\ \rho u_1 u_j + \delta_{1j} p \\ \rho u_2 u_j + \delta_{2j} p \\ \rho u_3 u_j + \delta_{3j} p \\ u_j (E + p) \end{pmatrix}, \quad \hat{\mathbf{F}}_{v,j} = \begin{pmatrix} 0 \\ \tau_{1j} \\ \tau_{2j} \\ \tau_{3j} \\ u_k \tau_{kj} - q_j \end{pmatrix}. \tag{2}$$

The total energy per unit mass E, the viscous stress tensor τ_{ij}, and the heat flux vector q_j are defined as

$$E = \frac{p}{\gamma - 1} + \frac{1}{2} \rho u_i u_i, \tag{3}$$

$$\tau_{ij} = \mu \left(\frac{\partial u_i}{\partial x_j} + \frac{\partial u_j}{\partial x_i} - \frac{2}{3} \delta_{ij} \frac{\partial u_k}{\partial x_k} \right), \tag{4}$$

$$q_j = -k \frac{\partial T}{\partial x_j}, \tag{5}$$

where μ is the fluid viscosity and k is the thermal conductivity. The system of equations is closed by the equation of state. Since the gas is calorically perfect, the equation of state is

$$p = \rho R T. \tag{6}$$

The gas is assumed to be air so the gas constant, R, has a value of 287.04 $\mathrm{m}^2/\mathrm{s}^2$ K, the ratio of the specific heats, γ, is 1.4 and the Prandtl number, Pr, is 0.72. The viscosity is computed using Sutherland's law in the form

$$\mu = \mu_r \left(\frac{T}{T_r} \right)^{1.5} \frac{T_r + T_s}{T + T_s} \tag{7}$$

where $\mu_r = 1.7894 \times 10^{-5}$ (N s)/m^2, $T_s = 110.33$ K, and $T_r = 288$ K. All variables are left in dimensional form.

The flow fields are obtained through direct numerical simulation of the governing equations. Before solving, the governing equations are transformed from the physical (x, y, z) space to a $(\xi, \eta, \zeta) = (\xi^1, \xi^2, \xi^3)$ computational space. The grid in the computational space is uniformly spaced with ξ, η, and ζ with each varying from 0 to 1. After the transformation, the governing equations become

$$\frac{\partial \mathbf{U}}{\partial t} + \frac{\partial \mathbf{F}_j}{\partial \xi^j} = \frac{\partial \mathbf{F}_{v,j}}{\partial \xi^j}, \quad j = 1, 2, 3 \tag{8}$$

where $\mathbf{U}$ is a vector of the conservative variables, $[\rho, \rho u, \rho v, \rho w, E]^T / J$. J is the determinate of the the Jacobian matrix:

$$J = \left| \frac{\partial (\xi, \eta, \zeta)}{\partial (x, y, z)} \right| \tag{9}$$

$\mathbf{F}_j$ and $\mathbf{F}_{v,j}$ are the vectors of the inviscid and viscous fluxes, respectively, in the jth direction of the computational space and are given as

$$\mathbf{F}_j = \frac{1}{J} \begin{pmatrix} \rho U_j \\ \rho u_1 U_j + \delta_{1j} \, \xi_1^j p \\ \rho u_2 U_j + \delta_{2j} \, \xi_2^j p \\ \rho u_3 U_j + \delta_{3j} \, \xi_3^j p \\ U_j (E + p) \end{pmatrix}, \quad \mathbf{F}_{v,j} = \frac{1}{J} \begin{pmatrix} 0 \\ \xi_k^j \, \tau_{1k} \\ \xi_k^j \, \tau_{2k} \\ \xi_k^j \, \tau_{3k} \\ \xi_k^j u_n \tau_{nk} - \xi_k^j \, q_k \end{pmatrix} \tag{10}$$

where $\xi_k^j \equiv \frac{\partial \xi^j}{\partial x_k}$ are the metrics and U_j is given by

$$U_j = u_k \, \xi_k^j. \tag{11}$$

The shear stresses and heat fluxes in curvilinear coordinates are

$$\tau_{ij} = \mu \left(\xi_j^k \frac{\partial u_i}{\partial \xi^k} + \xi_i^k \frac{\partial u_j}{\partial \xi^k} - \frac{2}{3} \, \delta_{ij} \, \xi_k^n \frac{\partial u_k}{\partial \xi^n} \right), \tag{12}$$

$$q_j = -k \, \xi_j^k \frac{\partial T}{\partial \xi^k}. \tag{13}$$

The inviscid terms in the governing equation are split using local Lax-Friedrichs flux splitting for upwinding.

$$\mathbf{F}_j = \mathbf{F}_j^+ + \mathbf{F}_j^- \tag{14}$$

where $\mathbf{F}_j^\pm$ is

$$\mathbf{F}_j^\pm = \tfrac{1}{2} \left(\mathbf{F}_j \pm \lambda_j \mathbf{U} \right) \tag{15}$$

and λ_j is

$$\lambda_j = \sqrt{(u_k \, \xi_k^j)^2 + \epsilon^2 c^2 \left((\xi_1^j)^2 + (\xi_2^j)^2 + (\xi_3^j)^2 \right)} + c \sqrt{(\xi_1^j)^2 + (\xi_2^j)^2 + (\xi_3^j)^2} \tag{16}$$

where c is the speed of sound and ϵ is 0.1.

The inviscid terms are computed using the fifth-order finite-difference WENO scheme of Jiang and Shu[22] but with some modifications. Jiang and Shu transform the fluxes into characteristic space before applying WENO. In this work, WENO is apply directly to the fluxes without the transformation. In addition, the weights used for all the fluxes are computed from the fluid density only. A third-order TVD[22] scheme was used for time advancement and the viscous terms were computed using sixth-order central finite differencing.

The geometry of the roughness was imposed with three different methods in this work. The first was with body-fitted grids. This is only possible when the roughness has a smooth geometry such as a Gaussian. The body-fitted results are mostly used to validate and evaluate the other methods. The second and third methods were the cut-cell method and continuous forcing immersed boundary method.

III.A. Cut-Cell Method

The cut-cell method used in this work comes from Duan et al.[23] Duan et al. developed a globally fourth-order method for simulating flows with non-body-conforming geometries. The method allows numerical simulations of flow over isolated roughness elements to be performed on simple Cartesian grids. The main idea behind the cut-cell method of Duan et al. is to switch to a non-uniform one-sided finite-difference stencil whenever the normally used stencil will cross the immersed boundary. A summary of the method will be presented here with the differences between the current implementation and the original implementation of Duan et al. pointed out.

III.A.1. Point Classification

The cut-cell method begins by classifying all the grid points as either a regular point, an irregular point, a dropped point, or a boundary point. Figure 1 shows the classification for a sample ξ grid line. The immersed boundary intersects the grid line at the point ξ_1. The solid is assumed to be to the left of ξ_1 and the fluid to the right. The point ξ_1 is classified as a boundary point. Boundary points are created anywhere the immersed surface crosses a grid line. Boundary points are not part of the original Cartesian grid. All the points to the left of ξ_1 are classified as dropped points. Dropped points are usually points within the immersed surface and should not be used in any of the calculations. The first point to the right of ξ_1 is classified as dropped in the ξ direction only. Although this point is in the fluid, the point is treated as a dropped point while performing computations in the ξ direction. The point was dropped because it was too close to the boundary point and its inclusion would severally limit the timestep size. The criteria for determining when a point is too close is based on a specified parameter Θ and will be explained later. ξ_2, ξ_3, and ξ_4 are all classified as irregular points. Irregular points are any points whose finite-difference stencil would normally include a dropped point. The points ξ_5 to ξ_8 are regular points. Regular points are any

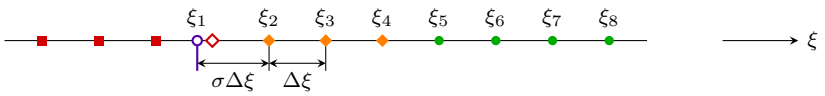

Figure 1. Point classification for ξ grid line with $\Theta \approx 1/3$. Immersed boundary ——; Regular point ●; Irregular point ◆; Boundary point ○; Dropped point ■; Dropped point in ξ direction only ◇.

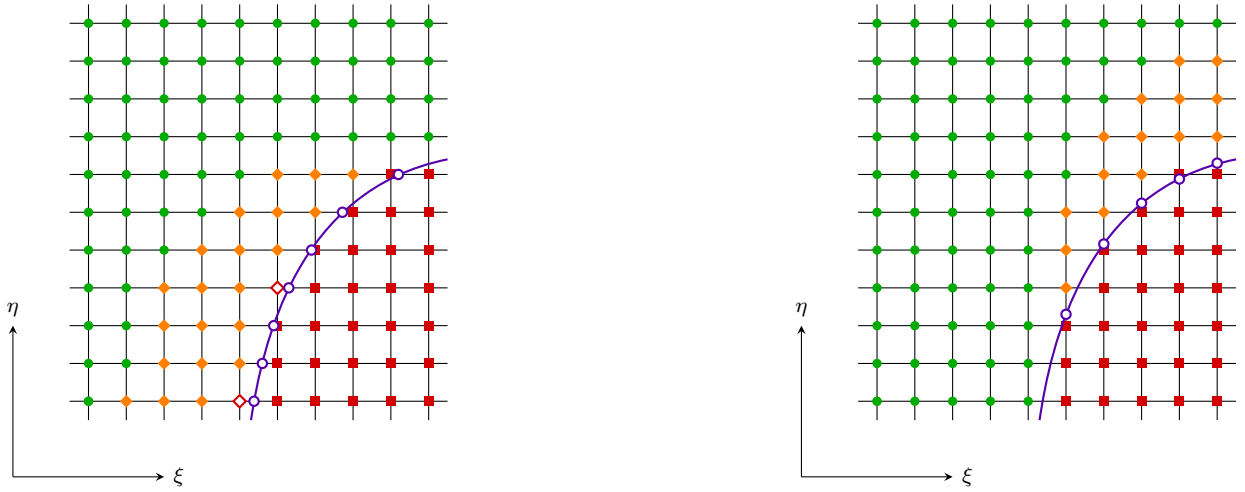

(a) Point classification for ξ direction

(b) Point classification for η direction

Figure 2. Point classification for two-dimensional computational space for $\Theta \approx 1/3$. Immersed boundary ——; Regular point ●; Irregular point ◆; Boundary point ○; Dropped point in both directions ■; Dropped point in specified direction only ◇.

points whose finite-difference stencil does not include any dropped points. When applying the method to two-dimensional and three-dimensional problems, a grid point may have a different classification in each of the computational directions. Figure 2 shows the point classification for a sample two-dimensional domain. The treatment for regular, irregular, boundary, and dropped points will be covered one at time.

III.A.2. Dropped Points

There are two different types of dropped points. The first type is when a point is dropped in all directions of the computational domain. Is this case, the point is never used in the calculations and therefore no special treatment is needed. All the points inside the immersed surface are of this type. The second type is when a point is dropped in at least one computational direction but not all of them. If the distance from a grid point to a boundary point along a grid line divided by the point spacing for that grid line is less than the specified value Θ, then the grid point is dropped in the direction of that grid line. For the fourth-order cut-cell method, Duan et al. recommend a value of 1.0 for Θ for all directions of the computational domain. In this work, separate Θ's were used in each of the directions. A value of 0.25 was used in the both ξ and ζ directions and a value of 0.75 was used in the η direction. In all the simulations performed here, the ξ, η, and ζ directions correspond to the streamwise, wall normal, and spanwise directions, respectively.

For the second type of dropped point, the point will not be used in stencils in the dropped direction(s) but can be used in the remaining direction(s). Due to this, the values at these points must be computed but they cannot be advanced in time like points which are regular or irregular in all the directions of the domain. Duan et al. interpolated the conservative flow variables at these points using a fourth-order interpolation along the grid line in one of the dropped direction. The interpolation stencil always includes the boundary point adjacent to the dropped point. In this work, the conservative flow variables at these points are computed using a second-order least-squares polynomial in x, y, and z of the form

$$\mathbf{U}(x,y,z) = c_1 + c_2\Delta x + c_3\Delta y + c_4\Delta z + c_5\Delta x\Delta y + c_6\Delta x\Delta z + c_7\Delta y\Delta z + c_8\Delta x^2 + c_9\Delta y^2 + c_{10}\Delta z^2 \quad (17)$$

where

$$\Delta x = x - x_d, \qquad \Delta y = y - y_d, \qquad \Delta z = z - z_d, \quad (18)$$

	$a^+_{i,1}$	$a^+_{i,2}$	$a^+_{i,3}$	$a^+_{i,4}$	$a^+_{i,5}$
$i=1$	$\frac{3}{2\sigma(\sigma+1)(\sigma+2)}$	$\frac{22\sigma-9}{12\sigma}$	$\frac{2-7\sigma}{6(\sigma+1)}$	$\frac{4\sigma-1}{12(\sigma+2)}$	0
$i=2$	$\frac{-1}{2\sigma(\sigma+1)(\sigma+2)}$	$\frac{4\sigma+3}{12\sigma}$	$\frac{5\sigma+2}{6(\sigma+1)}$	$\frac{-(2\sigma+1)}{12(\sigma+2)}$	0
$i=3$	$\frac{1}{2\sigma(\sigma+1)(\sigma+2)}$	$\frac{-(2\sigma+3)}{12\sigma}$	$\frac{5\sigma+8}{6(\sigma+1)}$	$\frac{4\sigma+5}{12(\sigma+2)}$	0
	$a^-_{i,1}$	$a^-_{i,2}$	$a^-_{i,3}$	$a^-_{i,4}$	$a^-_{i,5}$
$i=1$	0	$\frac{25}{12}$	$-\frac{23}{12}$	$\frac{13}{12}$	$-\frac{3}{12}$
$i=2$	0	$\frac{3}{12}$	$\frac{13}{12}$	$-\frac{5}{12}$	$\frac{1}{12}$

Table 1. One-sided non-uniform interpolation constants for inviscid terms at irregular points.

and x_d, y_d, and z_d are the x, y, and z values of the dropped point. The constants are computed from the 35 closest points by index to the dropped point. The 35 points can include regular, irregular, and boundary points. Other dropped points cannot be included in the 35 points. Including them in the interpolation will cause the flow variables at one dropped point to be related to the flow variables at all the other dropped points resulting in a large implicit system. By not including the other dropped points, the flow variables at each point may be computed individually.

In addition to computing the flow variables at points dropped in one or more directions, the shear stresses and heat fluxes must also be computed at these points. Duan et al. do not mention how they compute the shear stress and heat fluxes at these points. In this work, they are computed using a least-squares polynomial and the same 35 grid points as the conservative flow variables.

III.A.3. Regular Points

Regular points are grid points whose finite-difference stencil does not contain any dropped points. This allows the regular finite-difference stencils to used and hence does not require any special attention. In the original implementation by Duan et al., the fifth-order upwind scheme of Zhong[24] was used at regular points. In the current work, a fifth-order finite-difference WENO scheme is used at these points.

III.A.4. Irregular Points

Irregular points are any points whose normal finite-difference stencil includes dropped points. Since dropped points should not be used in the calculations, the finite-difference stencil for irregular points must be changed. For the irregular points ξ_2, ξ_3, and ξ_4 from Figure 1, Duan et al. change the stencil for the inviscid terms to a third-order or fourth-order one-sided non-uniform upwind finite-difference stencil. The stencils can include the boundary point at ξ_1. The inclusion of the boundary point is what makes the stencil non-uniform since the spacing between the boundary point and ξ_2 is $\sigma\Delta\xi$ instead of just $\Delta\xi$. In this work, the derivatives are first cast in conservative form and then the fluxes are interpolated using a non-uniform stencil. The derivative of the inviscid flux in the ξ direction with respect to ξ is computed as

$$\frac{\partial \mathbf{F}_\xi}{\partial \xi}(\xi_i) = \frac{\mathbf{F}^+_\xi(\xi_{i+1/2}) - \mathbf{F}^+_\xi(\xi_{i-1/2})}{\Delta\xi} + \frac{\mathbf{F}^-_\xi(\xi_{i+1/2}) - \mathbf{F}^-_\xi(\xi_{i-1/2})}{\Delta\xi}. \tag{19}$$

The fluxes at the half grid points are computed as

$$\mathbf{F}^\pm_\xi(\xi_{i+1/2}) = \sum_{j=1}^{5} a^\pm_{i,j}\, \mathbf{F}^\pm_\xi(\xi_j) \tag{20}$$

where the constants are given in Table 1. The fluxes at $\xi_{1+1/2}$ are not computed at the half way point between ξ_1 and ξ_2. They are instead evaluated at $\xi_2 - \Delta\xi/2$. The fluxes $\mathbf{F}^+_\xi(\xi_{4+1/2})$, $\mathbf{F}^-_\xi(\xi_{4+1/2})$, and $\mathbf{F}^-_\xi(\xi_{3+1/2})$ are computed using WENO since there are sufficient uniform points to form the WENO stencil.

	$a_{i,1}$	$a_{i,2}$	$a_{i,3}$	$a_{i,4}$	$a_{i,5}$	$a_{i,6}$	$a_{i,7}$
$i=1$	$\frac{-2(2\sigma+3)(\sigma^2+3\sigma+1)}{\sigma(\sigma+1)(\sigma+2)(\sigma+3)}$	$\frac{(\sigma+1)(\sigma+2)(\sigma+3)}{6\sigma}$	$\frac{-\sigma(\sigma+2)(\sigma+3)}{2(\sigma+1)}$	$\frac{\sigma(\sigma+1)(\sigma+3)}{2(\sigma+2)}$	$\frac{-\sigma(\sigma+1)(\sigma+2)}{6(\sigma+3)}$	0	0
$i=2$	$\frac{-6}{\sigma(\sigma+1)(\sigma+2)(\sigma+3)}$	$\frac{6-11\sigma}{6\sigma}$	$\frac{3\sigma}{(\sigma+1)}$	$\frac{-3\sigma}{2(\sigma+2)}$	$\frac{\sigma}{3(\sigma+3)}$	0	0
$i=3$	$\frac{2}{\sigma(\sigma+1)(\sigma+2)(\sigma+3)}$	$\frac{-2(\sigma+1)}{6\sigma}$	$\frac{1-\sigma}{2(\sigma+1)}$	$\frac{\sigma+1}{(\sigma+2)}$	$\frac{-(\sigma+1)}{6(\sigma+3)}$	0	0

Table 2. One-sided non-uniform finite-difference constants for viscous terms at irregular and boundary points.

	$a_{4,j}$
$j=1$	$\frac{-12}{\sigma(\sigma+1)(\sigma+2)(\sigma+3)(\sigma+4)(\sigma+5)}$
$j=2$	$\frac{\sigma+2}{20\sigma}$
$j=3$	$\frac{-(\sigma+2)}{2(\sigma+1)}$
$j=4$	$\frac{1-\sigma}{3(\sigma+2)}$
$j=5$	$\frac{\sigma+2}{(\sigma+3)}$
$j=6$	$\frac{-(\sigma+2)}{4(\sigma+4)}$
$j=7$	$\frac{\sigma+2}{30(\sigma+5)}$

Table 3. Central non-uniform finite-difference constants for viscous terms at irregular points.

To compute the viscous terms, Duan et al. use a fourth-order one-sided non-uniform finite-difference stencil at ξ_2 and ξ_3 and a fifth-order one-sided non-uniform finite-difference stencil at ξ_4. In this work, the same stencil is used for ξ_2 and ξ_3 but a sixth-order central non-uniform finite-difference stencil is used at point ξ_4. This was done to be consistent with the scheme used at the regular points. The derivative of the viscous flux in the ξ direction with respect to ξ at all three points can be expressed as

$$\frac{\partial \mathbf{F}_{v,\xi}}{\partial \xi}(\xi_i) = \frac{1}{\Delta\xi} \sum_{j=1}^{7} a_{i,j}\, \mathbf{F}_{v,\xi}(\xi_j) \tag{21}$$

where the constants are given in Tables 2 and 3. Table 2 also includes the constants for computing the derivative at the boundary point ξ_1. These values will be used in the next section.

III.A.5. Boundary Points

Boundary points are created anywhere a grid line crosses the immersed surface. The boundary conditions for the flow will be imposed at the boundary points. Since the immersed surface is always treated as a wall in this work and the flow is viscous, the no-slip boundary condition are imposed there. The temperature at the wall will depend on the temperature boundary condition for the problem and will be either isothermal or adiabatic in this work. The pressure at the boundary points will be extrapolated from the flow.

In Duan et al., a fourth-order extrapolation in the direction of the grid line which created the boundary point is used to compute the wall pressure. For adiabatic walls, only the temperature gradient in the direction of the grid line which created the boundary point is set to zero. In the current work, it was found that for two-dimensional simulations this method works for shorter roughness elements but can cause numerical instabilities for taller roughness elements. For the two-dimensional simulations presented here, the pressure at boundary points was extrapolated in the wall normal direction and adiabatic walls had the temperature gradient in the wall normal direction set to zero. For three-dimensional simulations, the wall normal extrapolation did not work either. A least-squares polynomial was used instead.

The pressure at boundary points is computed using a second-order least-squares polynomial in x, y, and

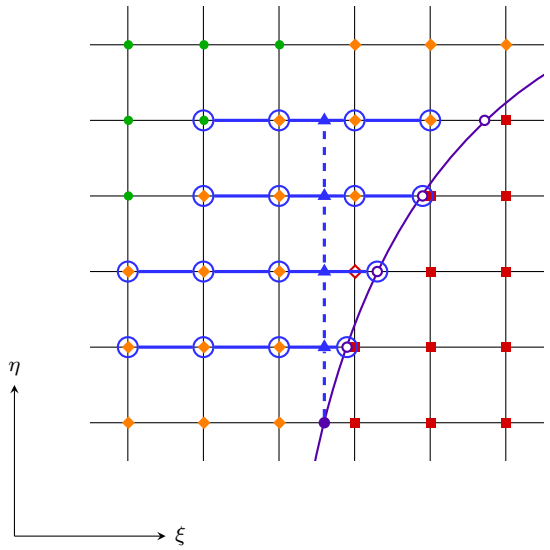

Figure 3. Points used to compute derivative in η direction for ξ boundary point. Point classification for the ξ direction with $\Theta \approx 1/3$ shown. Immersed boundary ——; Regular point ●; Irregular point ◆; Boundary point ○; Dropped point in both directions ■; Dropped point in ξ direction only ◇; Boundary point where derivative is being computed ●; Interpolated point for finite-difference stencil ▲; Stencil used to interpolate points for finite-difference stencil ○—○; Finite-difference stencil used to compute derivative ●- -▲.

z of the form

$$p(x,y,z) = c_1 + c_2\Delta x + c_3\Delta y + c_4\Delta z + c_5\Delta x\Delta y + c_6\Delta x\Delta z + c_7\Delta y\Delta z + c_8\Delta x^2 + c_9\Delta y^2 + c_{10}\Delta z^2 \quad (22)$$

where

$$\Delta x = x - x_b, \qquad \Delta y = y - y_b, \qquad \Delta z = z - z_b, \quad (23)$$

and x_b, y_b, and z_b are the x, y, and z values of the boundary point. The constants are computed using 25 regular or irregular points near the boundary point. The first three points along the grid line which created the boundary point should be included in the set of 25 points. Including these points reduces the likelihood of obtaining a singular matrix when computing the constants. The remaining 22 points are simply the closest points by index to the boundary point. Other boundary points cannot be included. Including them would result in a large implicit system. In addition, points dropped in any direction cannot be included. The least-squares polynomial used for points dropped in one or two directions includes boundary points and therefore must be updated after the boundary points.

A similar method is used to enforce the adiabatic boundary condition. A second-order polynomial for the temperature is created using the same 25 points. The polynomial is evaluated at four evenly space points in the wall normal direction. These values are then used along with a uniform fourth-order finite-difference stencil to enforce a zero temperature gradient at the wall.

In addition to imposing the boundary conditions on the flow variables, the shear stresses must be computed at the boundary points. To compute the shear stresses, derivatives are required in all the directions of the computational domain. To compute the require derivatives in the direction of the grid line which created the boundary point, Duan et al. use a fourth-order non-uniform finite-difference stencil. The same stencil is used in this work and is evaluated using Equation 21 with the constants coming from Table 2. However, Duan et al. do not explain how they compute the derivatives in the other directions of the computational domain. In this work, these derivatives are computed using a combination of interpolation and a uniform one-sided finite-difference stencil. Figure 3 shows how the derivative in η direction is computed for a boundary point defined by a ξ grid line in a two-dimensional domain. Four points above the boundary point are first compute by interpolating values in the ξ direction. The interpolation stencils should not include any points dropped in the direction of the grid line on which the boundary point lies (e.g. the ξ grid line in Figure 3). The interpolation stencil may include boundary points. These interpolated values are then used in a uniform one-side finite-difference stencil to compute the derivative.

III.B. Continuous Forcing IBM

In this work, the same continuous forcing immersed boundary method used by Marxen and Iaccarino[25] was implemented. The continuous forcing immersed boundary method mimics the immersed surface through a forcing term added to the right hand side of the governing equations. For two-dimensional simulations, the forcing term takes the form

$$\mathbf{B} = \begin{pmatrix} 0 \\ B_x \\ B_y \\ 0 \end{pmatrix} \tag{24}$$

where B_x and B_y enforce $u = 0$ and $v = 0$ on the immersed surface, respectively. Only the equations for B_x will be covered here. The expressions for B_y can be found by changing u to v in the following equations.

The forcing term B_x is a line integral of the product of a time-dependent body force, b_x, and an approximation to the delta function, d, along the immersed surface S,

$$B_x = \rho \oint_S b_x(\mathbf{x}_s)\, d(\mathbf{x} - \mathbf{x}_s)\, dS. \tag{25}$$

$\mathbf{x}$ is the location where the force is being computed and $\mathbf{x}_s$ is a location on the immersed surface. The line integral is evaluated using the trapezoidal rule. The approximation to the delta function is

$$d(\mathbf{x} - \mathbf{x}_s) = \exp\left\{ -\frac{(x - x_s)^2}{\sigma_x} - \frac{(y - y_s)^2}{\sigma_y} \right\}. \tag{26}$$

The body force is given by

$$b_x = \alpha \int_0^t u(\mathbf{x}_s, t')\, dt' + \beta u(\mathbf{x}_s, t) \tag{27}$$

where $u(\mathbf{x}_s, t)$ is the u velocity component evaluated at $\mathbf{x}_s$. Since the velocity is not solved for on the immersed surface, bilinear interpolation using the four neighboring grid points is used to compute $u(\mathbf{x}_s, t)$. The integral in the equation for b_x is computed as a Riemann sum.

III.C. Grid Generation and Boundary Conditions

In the current simulations, the roughness experiments in the Purdue wind tunnel are modeled as an isolated roughness located on a flat plate. This was done to simplify the grid generation process. Most of the grids that were used in this work were generated algebraically. The only exception is the tallest of the three-dimensional Gaussian roughnesses for the body-fitted grid and will be covered in section V.B. In all the simulations, the x axis is aligned with the flow direction and the y axis with the wall normal direction. In the three-dimensional simulations, the z axis is in the spanwise direction. The two-dimensional grids are clustered around the roughness element in the x direction and near the wall in the y direction. The same is true for the three-dimensional grids but they are also cluster around the roughness element in the z direction. For the three-dimensional simulations with hyperbolic tangent and Gaussian roughnesses, the grid is generated by the following equations:

$$x = (x_c - x_{in}) \left(1 + \frac{\sinh(a_1)}{\sinh(a_2)} \right) + x_{in} \tag{28}$$

$$y = (H - h(x, z)) \frac{\sinh(S_\eta \eta)}{\sinh(S_\eta)} + h(x, z) \tag{29}$$

$$z = \begin{cases} W \dfrac{\sinh(S_\zeta \zeta)}{\sinh(S_\zeta)} & \text{when simulating half domain in } z \\ W \dfrac{\sinh(S_\zeta (2k/KL - 1))}{\sinh(S_\zeta)}, \quad k = 1, \ldots, KL & \text{when simulating full domain in } z \end{cases} \tag{30}$$

where KL is the number of points in the ζ direction and

$$\begin{aligned} a_1 &= S_\xi \xi - \tfrac{1}{2}\log\left(\frac{b_+}{b_-}\right), \\ a_2 &= \tfrac{1}{2}\log\left(\frac{b_+}{b_-}\right), \\ b_\pm &= 1 + (\exp(\pm S_\xi) - 1)\,\frac{x_c - x_{in}}{x_{out} - x_{in}}. \end{aligned} \tag{31}$$

x_{in} and x_{out} are the x locations of the domain inlet and outlet, respectively. x_c is the center of the clustering in the x direction. H is the domain height and W is the domain half width. For the body-fitted grids, $h(x,z)$ is the function governing the roughness geometry. For the cut-cell method and the continuous forcing immersed boundary method, $h(x,z)$ is simply zero. S_ξ, S_η, and S_ζ control the amount of clustering in the x, y and z directions, respectively. The same equations are used to generate the two-dimensional grids but z is set to zero and the function governing the roughness geometry is only a function of x.

When simulating cylindrical roughness elements, a different point distribution is used in the y direction. The distribution has the form

$$y = H\left[y_{sinh}\eta^P + y_{lin}\left(1 - \eta^P\right)\right] \tag{32}$$

where

$$\begin{aligned} y_{lin} &= L\eta, \\ y_{sinh} &= y_c\left(1 + \frac{\sinh(c_1)}{\sinh(c_1)}\right), \\ c_1 &= S_\eta\eta - \tfrac{1}{2}\log\left(\frac{d_+}{d_-}\right), \\ c_2 &= \tfrac{1}{2}\log\left(\frac{d_+}{d_-}\right), \\ d_\pm &= 1 + (\exp(\pm S_\eta) - 1)\,\frac{y_c}{H}. \end{aligned} \tag{33}$$

Equation 32 produces a uniform distribution near the wall and a hyperbolic sine distribution away from the wall. P controls the extent of the linear region while L controls the clustering in this region. y_c is the center of the clustering in the y direction for the hyperbolic sine region.

The leading edge of the flat plate is not included in any of the simulations. Instead, a compressible similarity solution is imposed at the inlet of the numerical domain and held fixed with time. The outlet of the domain is a supersonic outlet so the conservative variables are extrapolated from the interior of the domain. At the top of the domain, a sponge layer[26] is used to prevent the shock and expansion fan created by the roughness from reflecting back into the domain. The bottom edge of the domain is a no-slip wall with the pressure being extrapolated from the domain interior. The temperature on the wall is either adiabatic or isothermal and depends on the problem. For the three-dimensional case, symmetry boundary conditions used at both edges on the domain in the z direction.

IV. Two-Dimensional Results

IV.A. Hyperbolic Tangent Roughness

The first two-dimensional simulation comes from Marxen and Iaccarino.[25] Marxen and Iaccarino simulated Mach 4.8 boundary-layer flow over an isolated roughness constructed from hyperbolic tangent curves located on a flat plate. The roughness height to undisturbed boundary-layer thickness ratio (k/δ) is 0.547. The origin of the coordinate system is located at the leading edge of the flat plate but the leading edge was not included in the simulations. The freestream conditions for the flow are summarized in Table 4 where $Re_\infty = \rho_\infty u_\infty L_{ref}/\mu_\infty$. The equation for the roughness geometry can be found in Marxen and Iaccarino. The results were computed with a body-fitted grid, the cut-cell method, and the continuous forcing immersed boundary method. The purpose of this simulation was to evaluate and compare the cut-cell method and the continuous forcing immersed boundary method since only one method would be used for the remaining

Freestream Mach number	M_∞	4.8
Freestream velocity	u_∞	720 m/s
Freestream pressure	p_∞	239.426 Pa
Freestream temperature	T_∞	55.4 K
Freestream density	ρ_∞	1.51×10^{-2} kg/m^3
Freestream Reynolds number	Re_∞	10^5
Reference length	L_{ref}	3.365×10^{-2} m
Roughness height	k	$0.1L_{ref}$
Ratio of roughness height to boundary-layer thickness	k/δ	0.547

Table 4. Flow conditions for hyperbolic tangent simulations

α	β	σ_x	σ_y
$-10^5 \frac{c_\infty^2}{L_{ref}^3}$	$-5\times10^5 \frac{c_\infty}{L_{ref}^2}$	$3.2\times10^{-4}\,L_{ref}$	$5\times10^{-4}\,L_{ref}$

Table 5. Constants for continuous forcing immersed boundary method

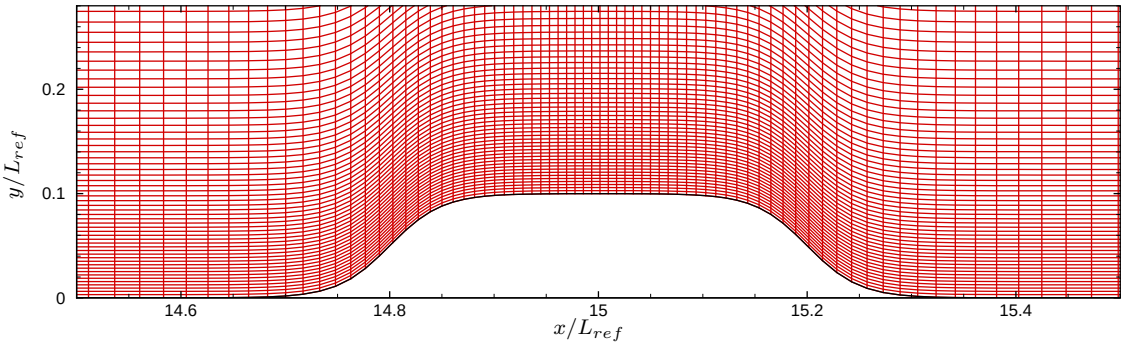

(a) Body-fitted grid

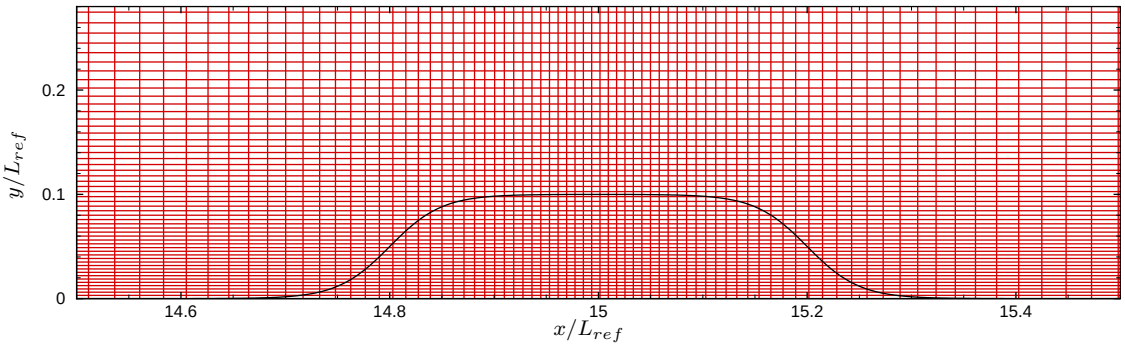

(b) Cartesian grid used for cut-cell method. Roughness element shown in black.

Figure 4. Grid in vicinity of the two-dimensional hyperbolic tangent roughness element. Both grids use 800 points in the x direction and 400 points in the y direction. Every fourth point in both directions shown.

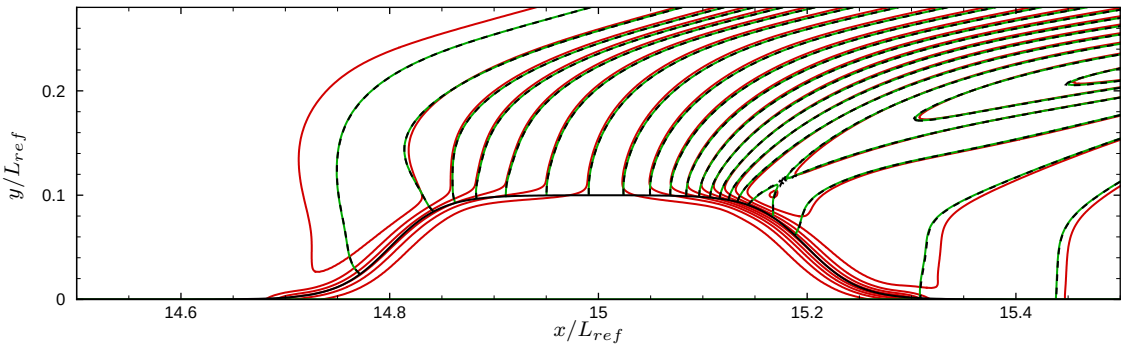

(a) Pressure contour. Non-dimensionalized as p/p_∞. 18 levels from 0.45 to 1.3.

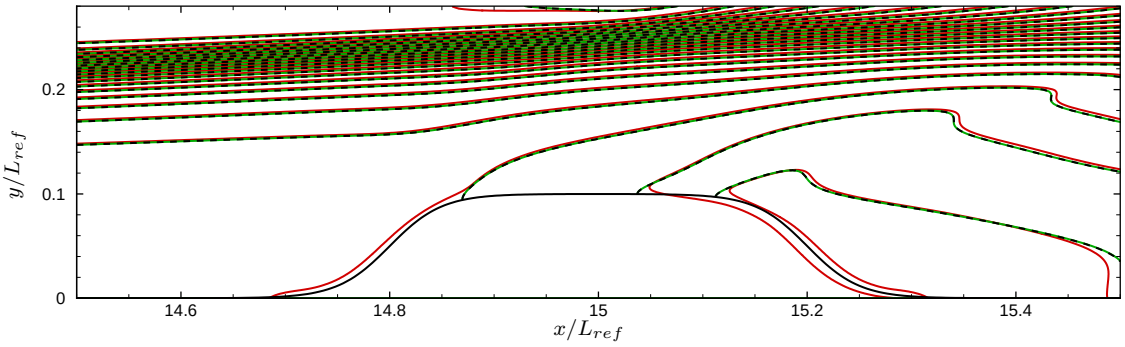

(b) Density contour. Non-dimensionalized as ρ/ρ_∞. 22 levels from 0.15 to 1.2.

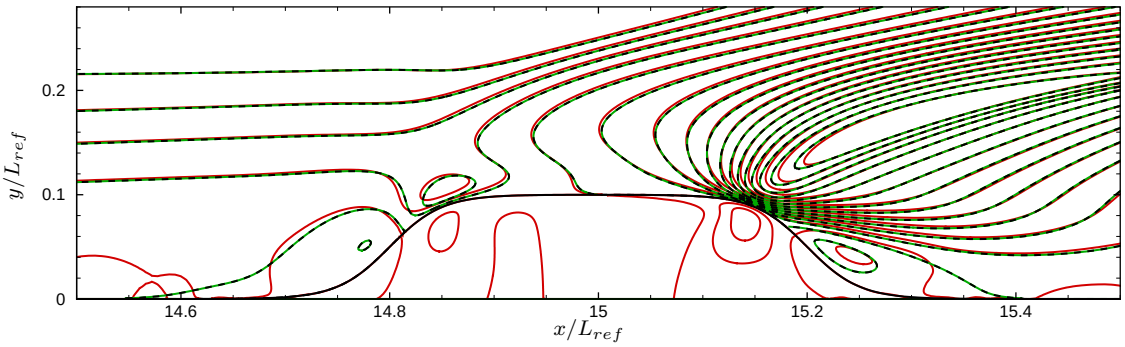

(c) v velocity contour. Non-dimensionalized as v/u_∞. 17 levels from -0.12 to 0.04.

Figure 5. Contours in vicinity of the two-dimensional hyperbolic tangent roughness element. Continuous forcing immersed boundary method ——; Cut-cell method ——; Body-fitted - - -.

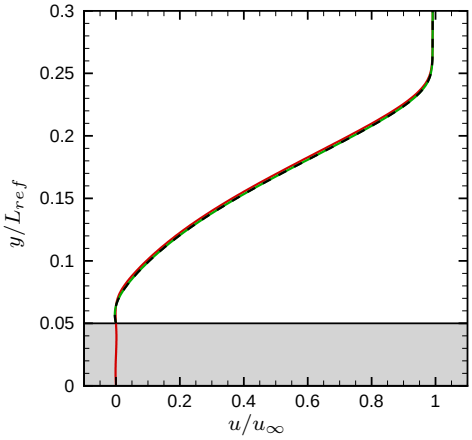

(a) Streamwise velocity at $x/L_{ref} = 14.8$

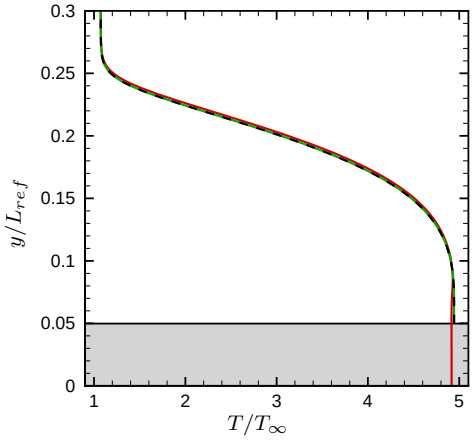

(b) Temperature at $x/L_{ref} = 14.8$

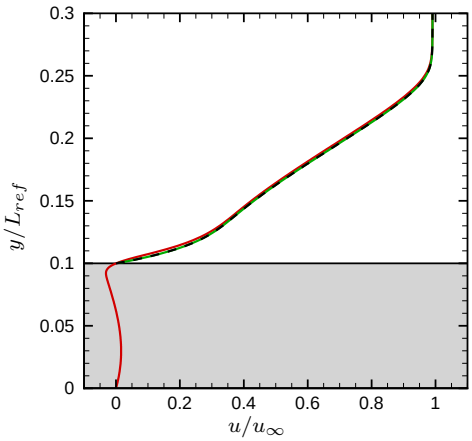

(c) Streamwise velocity at $x/L_{ref} = 15.0$

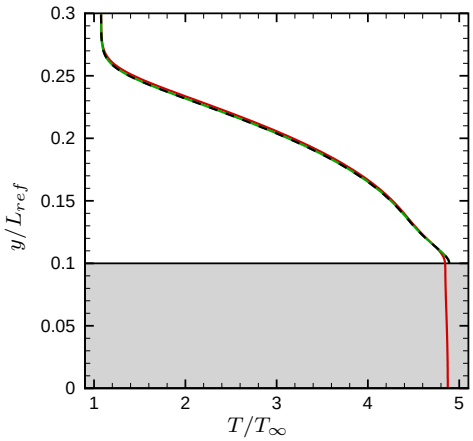

(d) Temperature at $x/L_{ref} = 15.0$

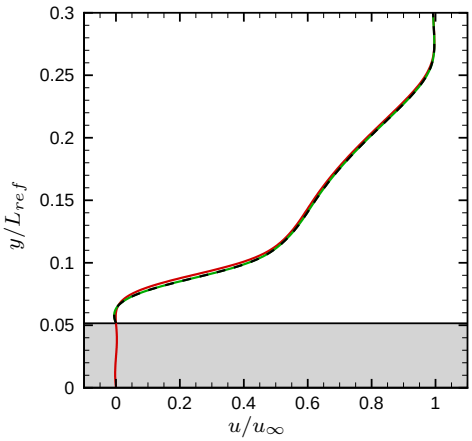

(e) Streamwise velocity at $x/L_{ref} = 15.2$

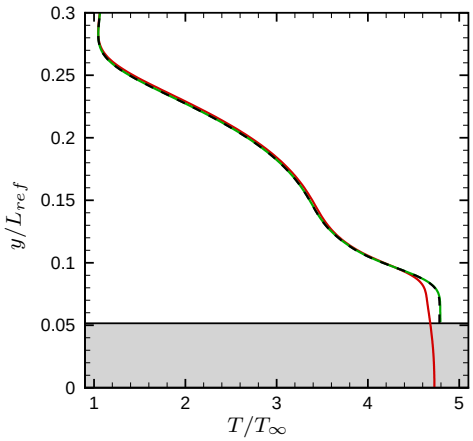

(f) Temperature at $x/L_{ref} = 15.2$

Figure 6. Streamwise velocity and temperature profiles for two-dimensional hyperbolic tangent roughness element. Roughness element shown in grey. Continuous forcing immersed boundary method ——; Cut-cell method ——; Body-fitted - - -.

Freestream Mach number	M_∞	5.93
Freestream velocity	u_∞	873 m/s
Freestream pressure	p_∞	0.37 kPa
Freestream temperature	T_∞	53.9 K
Stagnation pressure	p_0	551.58 kPa
Stagnation temperature	T_0	433 K
Wall temperature	T_{wall}	298.2 K
Freestream unit Reynolds number	Re_∞	5.94×10^6 m^{-1}
Undisturbed boundary-layer thickness	δ	9.23 mm

Table 6. Flow conditions for Gaussian and cylinderical roughness simulations

simulations in this study. The body-fitted results are used as a basis for the comparison between the cut-cell method and continuous forcing immersed boundary method. The two-dimensional roughness from Marxen and Iaccarino was chosen because Marxen and Iaccarino were able to simulated the roughness with the continuous forcing immersed boundary method showing that it could be done.

The grids in the vicinity of the roughness element for the body-fitted and cut-cell method are shown in Figure 4. The grids use 800 points in the x direction and 400 points in the y direction with $S_\xi = 10$, $S_\eta = 3.6$, and $x_c = 15L_{ref}$. The numerical domain starts at $x/L_{ref} = 5.859$ and ends at $x/L_{ref} = 30.1665$. The top of the domain is located at $y/L_{ref} = 1.575$. The grid used for the continuous forcing immersed boundary method is the same as the cut-cell method grid except 600 points are used in the y direction. The constants used in the continuous forcing immersed boundary method are shown in Table 5.

Figure 5 shows contour plots of pressure, density and v velocity in the vicinity of the roughness element for the three methods. The results from the body-fitted grid and the cut-cell method match exactly. Both results were confirmed to be grid convergence by increasing the grids points in the x direction to 1200 and the points in the y direction to 600. There were no visible changes in the results. The results from the continuous forcing immersed boundary method appear similar to the body-fitted results away from the roughness but there are significant differences near the roughness. The continuous forcing immersed boundary method results were not checked for grid convergence due to the method's low spatial convergence rate.

Figure 6 shows streamwise velocity and temperature profiles at various x/L_{ref} locations for the three methods. The profiles are at the upstream curved portion of the roughness ($x/L_{ref} = 14.8$), the center of the roughness ($x/L_{ref} = 15$) and the downstream curved portion of the roughness ($x/L_{ref} = 15.2$). Just as with the contours, the profiles for the body-fitted grid and cut-cell method match. There are noticeable differences between the body-fitted and continuous forcing immersed boundary method which are greatest near the roughness. Based on the results of this test, it was decided to use the cut-cell method for the remainder of the simulations in this study.

IV.B. Gaussian Roughness

The second two-dimensional simulation is Mach 6 flow over a Gaussian roughness with a k/δ ratio of 0.75. The purpose of the simulation is to test the cut-cell method under flow conditions similar to the Purdue wind tunnel. The flow conditions match those provided by Wheaton and Schneider[19] and are given in Table 6. The simulation has an isothermal wall with the temperature coming from Schneider.[27] A Gaussian roughness was used instead of a rectangular roughness (which would be a two-dimensional version of the cylindrical roughness) to allow body-fitted simulations to also be performed for comparison. The shape of the roughness is given as $h(x) = k\exp\left(-\frac{x^2}{r^2}\right)$ where k is the roughness height and r controls the roughness width. r is set to 0.498δ in this simulation. The Reynolds number based on the roughness height and the local conditions in the undisturbed boundary layer ($Re_k = \rho u k/\mu$) is 3,330.

The origin of the domain is located at the center of the roughness element. The numerical domain starts 40δ upstream of the roughness and ends 25δ downstream of the roughness. The domain has a height of 8.0δ. The grids in the vicinity of the roughness element for the body-fitted and cut-cell method are shown in Figure 7. The grids use 1200 points in the x direction and 800 points in the y direction with $S_\xi = 11$, $S_\eta = 2.9$, and $x_c = 0$. The solutions were not checked for grid convergence. However, very dense grids were

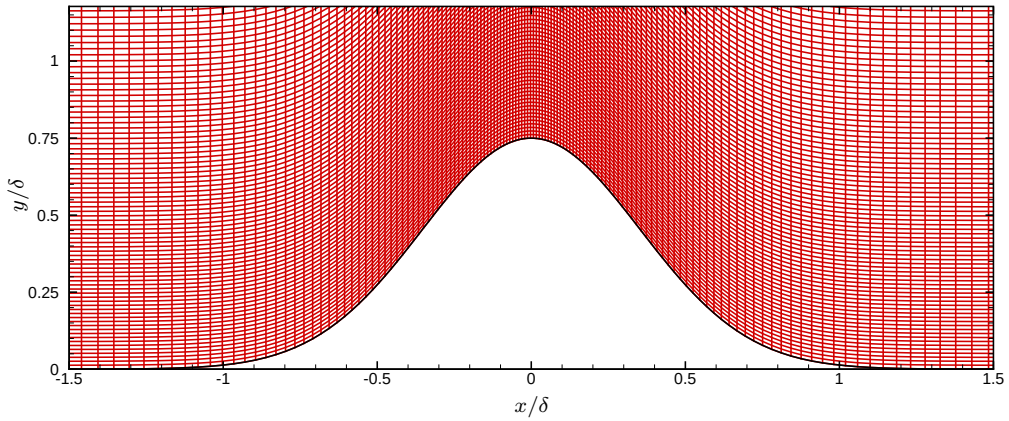

(a) Body-fitted grid

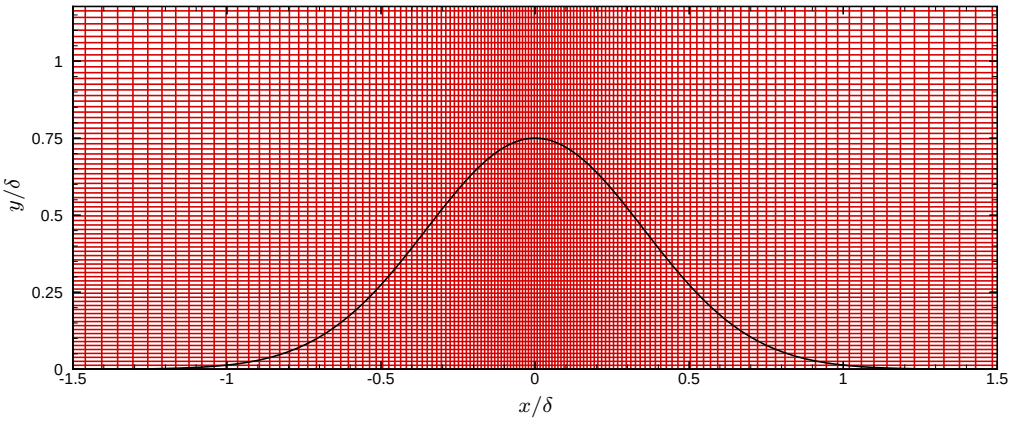

(b) Cartesian grid used for cut-cell method. Roughness element shown in black.

Figure 7. Grid in vicinity of the two-dimensional Gaussian roughness element. Both grids use 1200 points in the x direction and 800 points it the y direction. Every fourth point in both directions shown.

used so it is likely that the solutions are close to being grid converged.

Figure 8 shows contour plots of pressure, density, and v velocity in the vicinity of the roughness element for the body fitted grid and cut-cell method. The results from the two methods match very well. There appears to be a small difference between the pressure and density contours from the two methods near $x/\delta = 0.35$. Profiles of density and pressure at that x location are plot in Figure 9. Although the contours show a small difference, the profiles match. Figure 10 shows streamwise velocity and temperature profiles at various x/δ locations for the two methods. The profiles are at $x/\delta = -0.5$, $x/\delta = 0.0$, and $x/\delta = 0.5$. The profiles from the cut-cell method match exactly with the results from the body-fitted grid.

V. Three-Dimensional Results

V.A. Hyperbolic Tangent Roughness

The first three-dimensional roughness is a three-dimensional version of the hyperbolic tangent roughness from the two-dimensional results. This roughness was also simulated by Marxen and Iaccarino.[28] The equation for the roughness geometry is given in Marxen and Iaccarino. The roughness height and flow conditions match those of the two-dimensional simulation and are given in Table 4. The results were computed using a body-fitted grid and the cut-cell method. The purpose of the simulation was to evaluate the performance of the cut-cell method with a three-dimensional roughness.

For both the body-fitted grid and the cut-cell method, both sides of the roughness in the z direction were simulated. The grid in the vicinity of the roughness for the body-fitted grid and cut-cell method are shown in Figures 11 and 12, respectively. Both grids use 600 points in the x direction, 300 points in the y

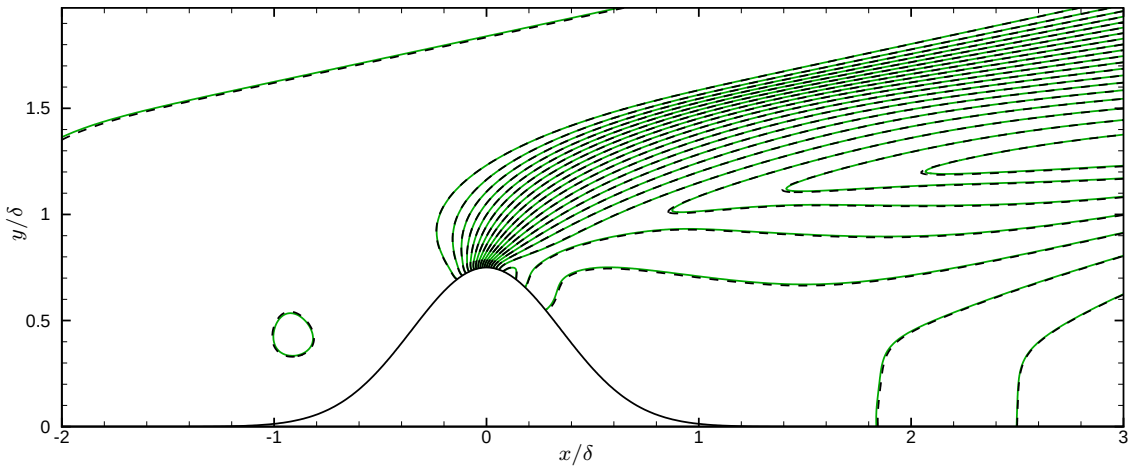

(a) Pressure contour. Non-dimensionalized as p/p_∞. 21 levels from 0.3 to 1.3.

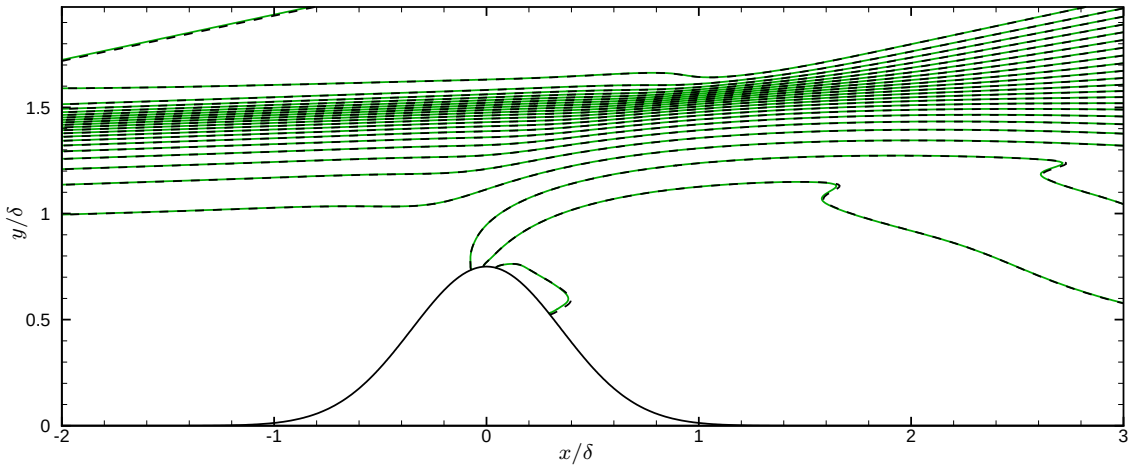

(b) Density contour. Non-dimensionalized as ρ/ρ_∞. 23 levels from 0.1 to 1.2.

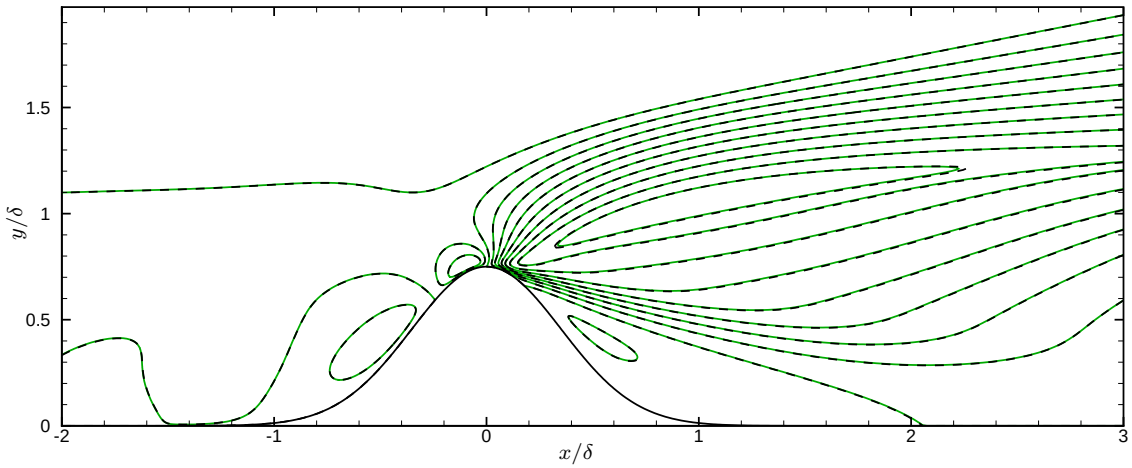

(c) v velocity contour. Non-dimensionalized as v/u_∞. 11 levels from -0.16 to 0.04.

Figure 8. Contours in vicinity of the two-dimensional Gaussian roughness element. Cut-cell method ——; Body-fitted - - -.

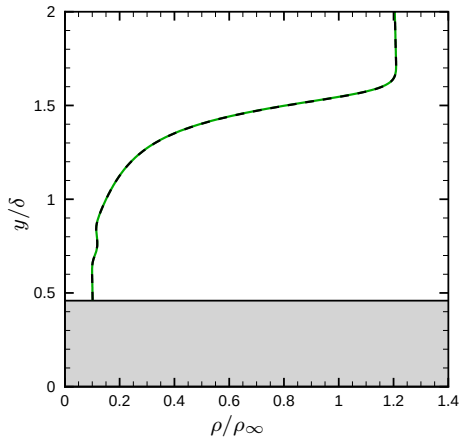

(a) Density at $x/\delta = 0.35$

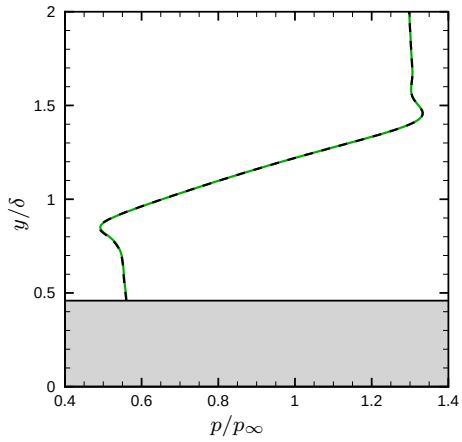

(b) Pressure at $x/\delta = 0.35$

Figure 9. Streamwise velocity and temperature profiles for two-dimensional Gaussian roughness element. Roughness element shown in gray. Cut-cell method ——; Body-fitted - - -.

direction, and 300 points in the z direction with $S_\xi = 10$, $S_\eta = 3.6$, $S_\zeta = 2$, and $x_c = 15L_{ref}$. The numerical domain starts at $x/L_{ref} = 10.6065$ and ends at $x/L_{ref} = 28.1665$. The top of the domain is located at $y/L_{ref} = 1.575$ and the half width is $W = 0.7L_{ref}$.

Contours of the pressure and the v velocity component near the roughness at the $z/L_{ref} = 0$ plane are shown in Figure 13 for the body-fitted grid and cut-cell method. The $z/L_{ref} = 0$ plane passes through the center of the roughness in the z direction. Contours of the pressure and the w velocity component near the roughness at the $x/L_{ref} = 15$ plane are shown in Figure 14. The $x/L_{ref} = 15$ plane passes through the center of the roughness in the x direction. The results from the two methods agree very well. Only small differences between the body-fitted and cut-cell results are visible. Neither set of results were confirmed to be grid converged. Increasing the grid resolution may remove the differences.

Figure 15 shows streamwise velocity and temperature profiles at various x/L_{ref} locations from the $z/L_{ref} = 0$ plane for the two methods. The profiles are at $x/L_{ref} = 14.8$, $x/L_{ref} = 15$, and $x/L_{ref} = 15.2$. The profiles from the two methods match except near the wall in the temperature profiles. Despite the small differences, the cut-cell method appears to work very well for this test case.

V.B. Gaussian Roughness

While the cut-cell code was being developed, a series of simulations were performed of flow over a flat plate with a three-dimensional Gaussian roughness using a body-fitted grid. Four different roughness heights were used with the tallest matching that of Wheaton and Schneider. The flow conditions match those of Wheaton and Schneider and are given in Table 6.

In these simulations, the origin of the numerical domain is located at the center of the roughness element. The numerical domain starts 20δ upstream of the roughness and ends 25δ downstream of the roughness. The domain has a height and half width of 5δ each. The shape of the roughness is given as $h(x,z) = k\exp\left(-\frac{x^2+z^2}{r^2}\right)$ where k is the roughness height and r controls the roughness width. Four different roughness heights were simulated. The tallest element has a k/δ ratio of 1.10 and is the same height as the roughness from Wheaton and Schneider. The remaining roughness elements have k/δ ratios of 0.75, 0.50, and 0.25. The shortest roughness element is completely submerged in the subsonic portion of the undisturbed boundary layer. r is set to 0.498δ for all the roughnesses. Figure 16 shows a comparison of the roughness elements used in the simulations to the roughness from Wheaton and Schneider. The height of the undisturbed boundary layer and the location where the Mach number is one (sonic line) are also shown. The Re_k for each roughness are listed in Table 7.

Two different grid generation techniques were used in the simulations. For the three shorter roughnesses, the grids were generated algebraically using the equations from section III.C. Figure 17 shows the grid in the vicinity of the $k/\delta = 0.75$ roughness. All the grids were generated with $S_\xi = 9$, $S_\eta = 2$, $S_\zeta = 4$, and $x_c = 0$. The grid for the $k/\delta = 1.10$ roughness element was generated using the method of Spekreijse.[29] Spekreijse

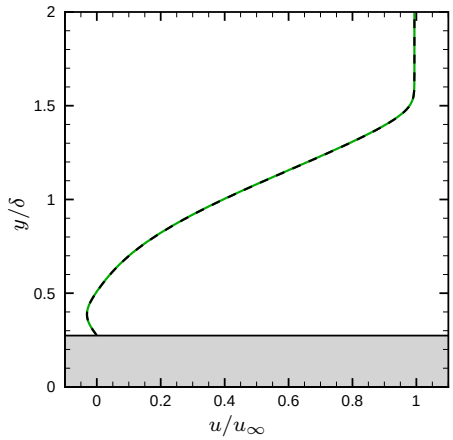

(a) Streamwise velocity at $x/\delta = -0.5$

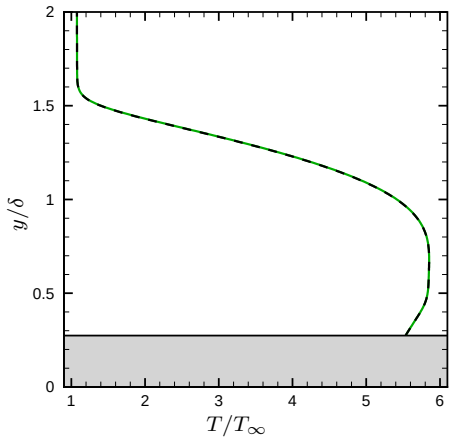

(b) Temperature at $x/\delta = -0.5$

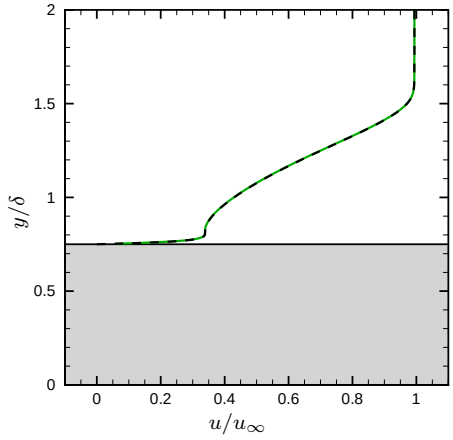

(c) Streamwise velocity at $x/\delta = 0.0$

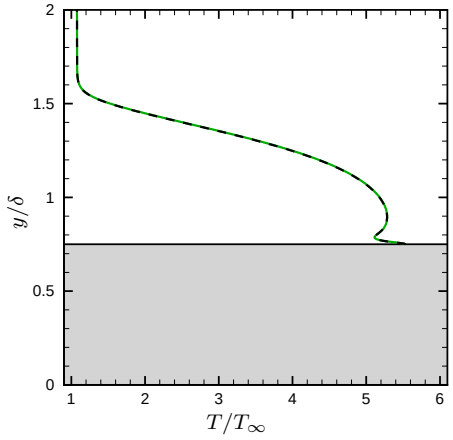

(d) Temperature at $x/\delta = 0.0$

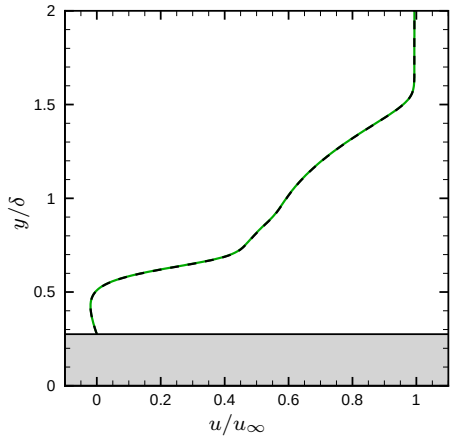

(e) Streamwise velocity at $x/\delta = 0.5$

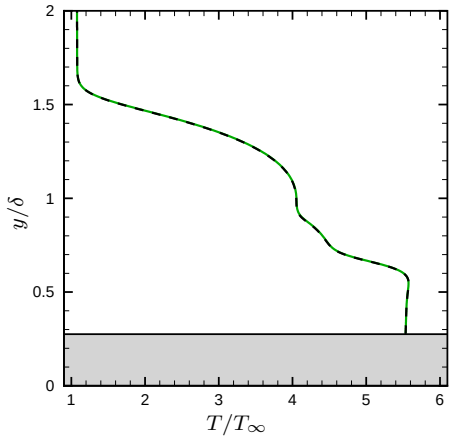

(f) Temperature at $x/\delta = 0.5$

Figure 10. Streamwise velocity and temperature profiles for two-dimensional Gaussian roughness element. Roughness element shown in gray. Cut-cell method ——; Body-fitted - - -.

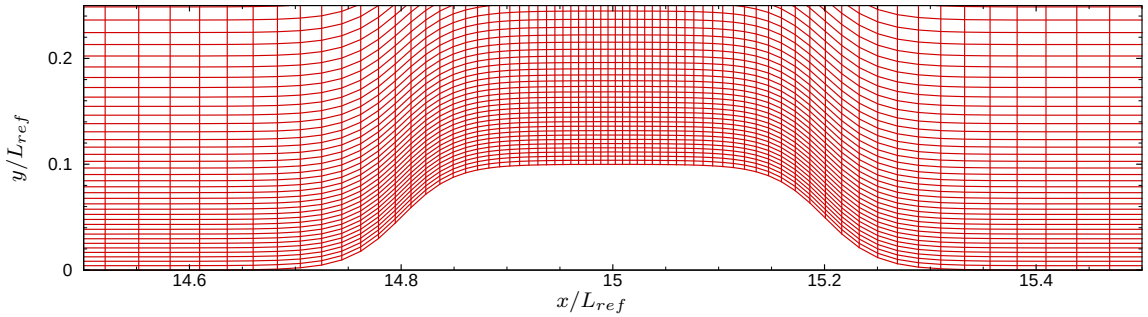

(a) $x - y$ plane at $z/L_{ref} = 0$

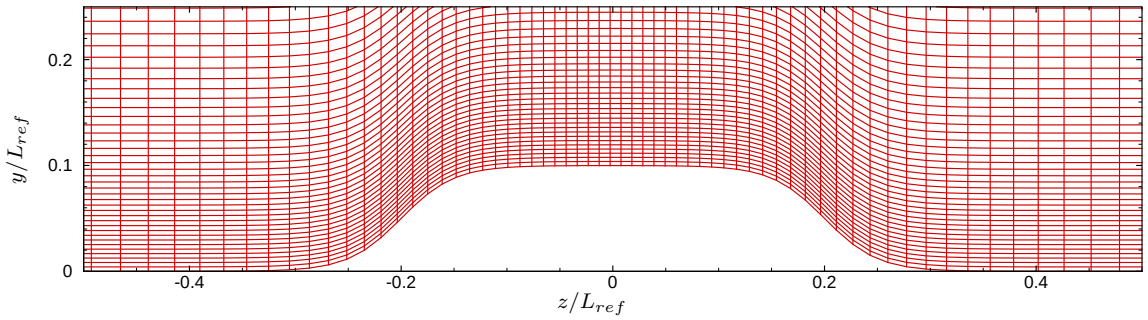

(b) $y - z$ plane at $x/L_{ref} = 15$

Figure 11. Body-fitted grid in the vicinity of the three-dimensional hyperbolic tangent roughness element. Grid has 600 points in x direction, 300 points in y direction, and 300 points in z direction. Every fourth point shown in all directions.

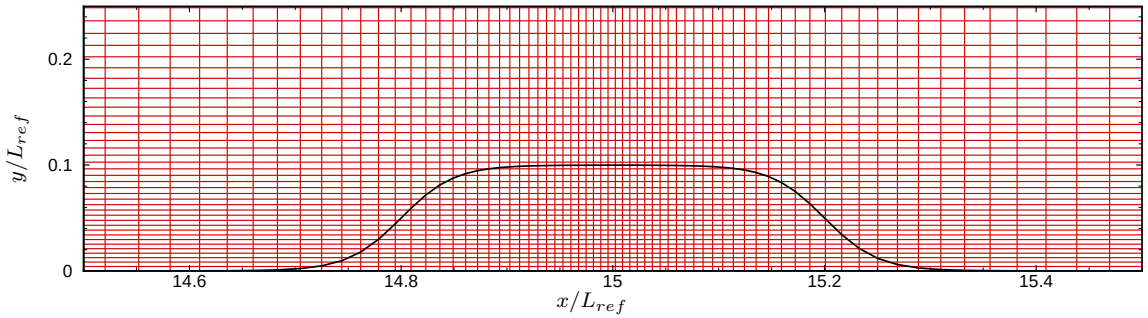

(a) $x - y$ plane at $z/L_{ref} = 0$

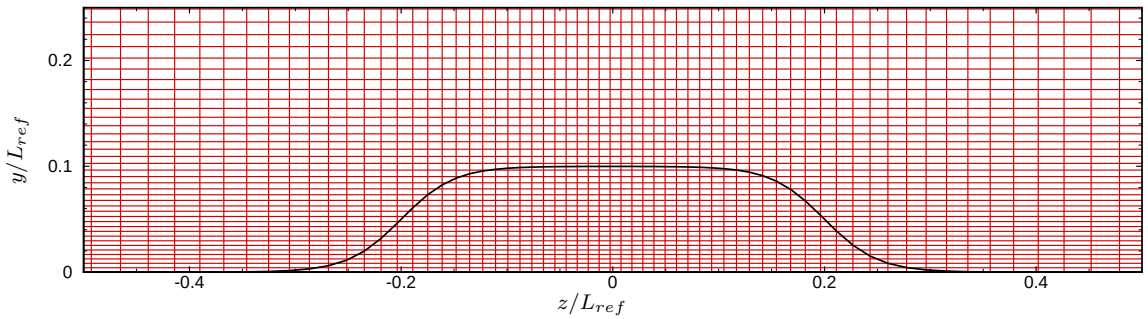

(b) $y - z$ plane at $x/L_{ref} = 15$

Figure 12. Grid in the vicinity of the three-dimensional hyperbolic tangent roughness element for cut-cell method. Roughness element shown in black. Grid has 600 points in x direction, 300 points in y direction, and 300 points in z direction. Every fourth point shown in all directions.

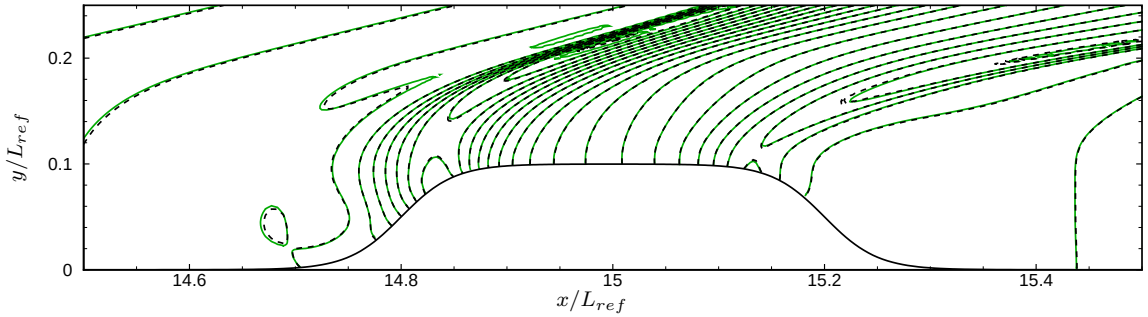

(a) Pressure contour. Non-dimensionalized as p/p_∞. 24 levels from 0.45 to 1.6.

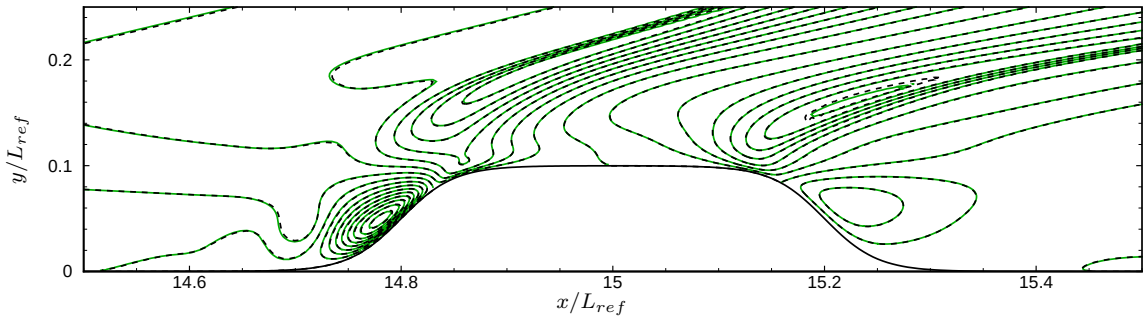

(b) v velocity contour. Non-dimensionalized as v/u_∞. 16 levels from -0.08 to 0.07.

Figure 13. Contours in vicinity of three-dimensional hyperbolic tangent roughness element at $z/L_{ref} = 0$ plane. Cut-cell method ——; Body-fitted - - -.

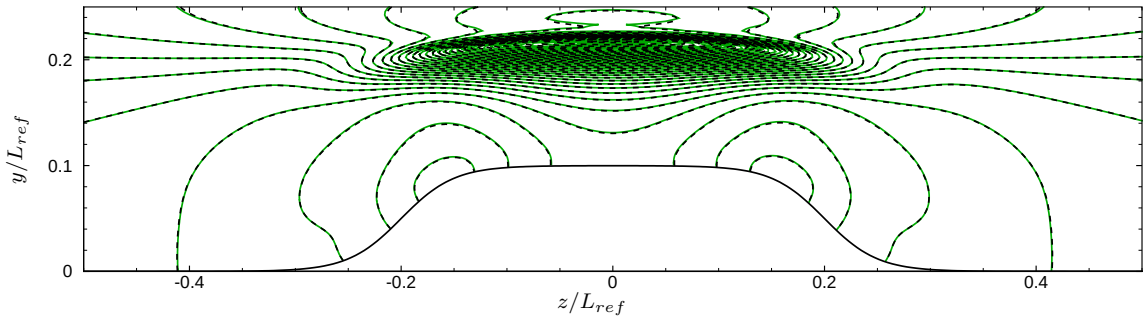

(a) Pressure contour. Non-dimensionalized as p/p_∞. 34 levels from 0.96 to 1.62.

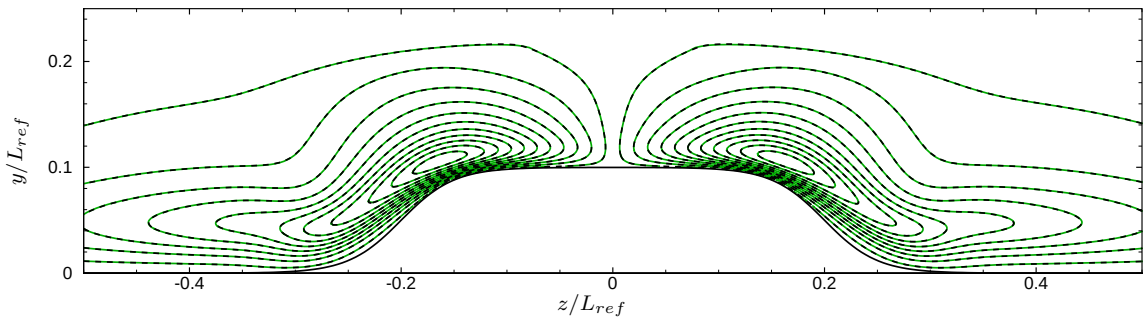

(b) w velocity contour. Non-dimensionalized as w/u_∞. 22 levels from -0.1 to 0.1.

Figure 14. Contours in vicinity of three-dimensional hyperbolic tangent roughness element at $x/L_{ref} = 15$ plane. Cut-cell method ——; Body-fitted - - -.

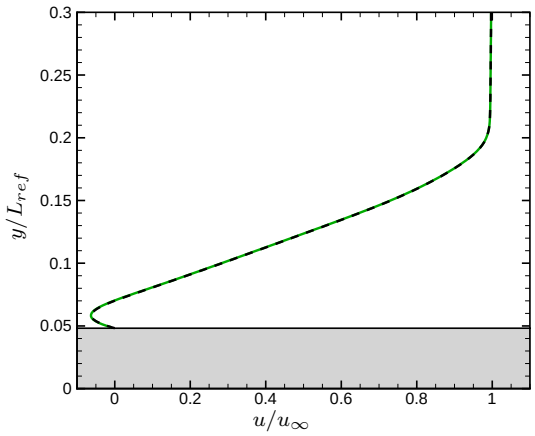

(a) Streamwise velocity at $x/L_{ref} = 14.8$

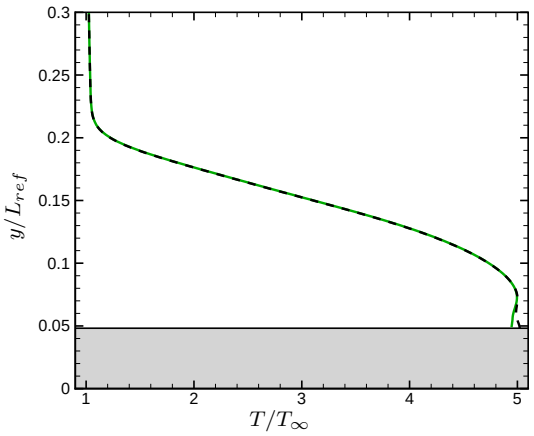

(b) Temperature at $x/L_{ref} = 14.8$

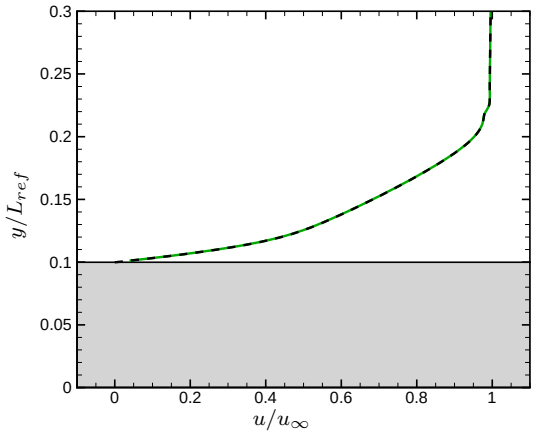

(c) Streamwise velocity at $x/L_{ref} = 15.0$

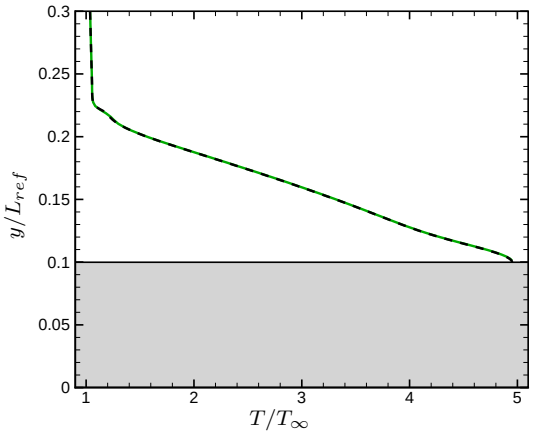

(d) Temperature at $x/L_{ref} = 15.0$

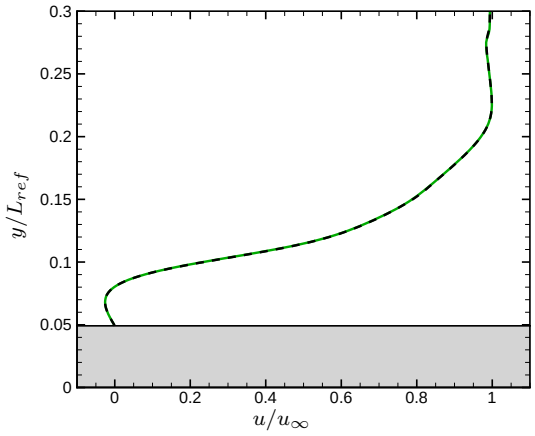

(e) Streamwise velocity at $x/L_{ref} = 15.2$

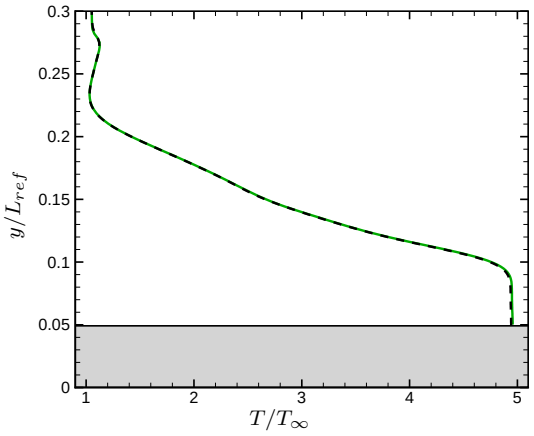

(f) Temperature at $x/L_{ref} = 15.2$

Figure 15. Streamwise velocity and temperature profiles for three-dimensional hyperbolic tangent roughness element. All profiles are from $z/L_{ref} = 0$ plane. Roughness element shown in grey. Cut-cell method ——; Body-fitted - - -.

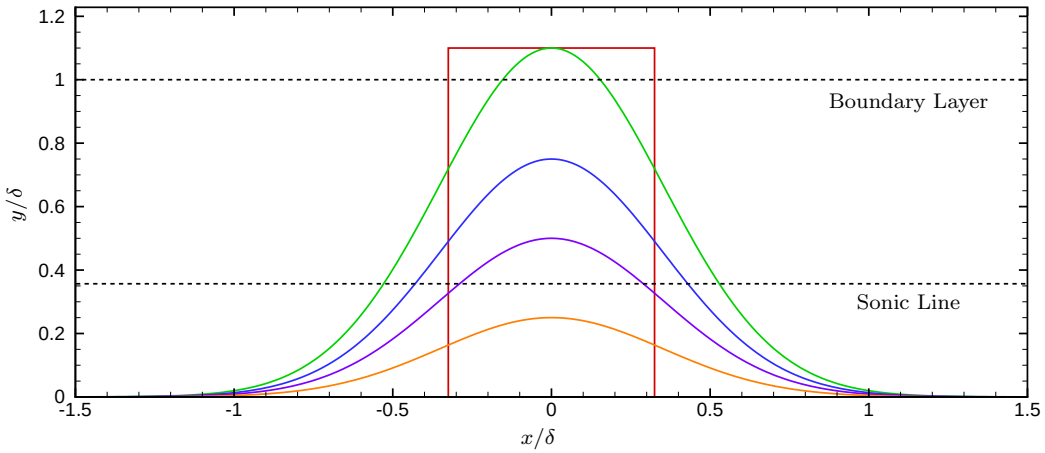

Figure 16. Comparison of roughness elements used in simulations to roughness used in Wheaton and Schneider.[19] k/δ = 1.10 Gaussian ——; k/δ = 0.75 Gaussian ——; k/δ = 0.50 Gaussian ——; k/δ = 0.25 Gaussian ——; k/δ = 1.10 cylinder from Wheaton and Schneider ——.

Roughness height (k/δ)	Roughness Reynolds Number (Re_k)
0.25	130
0.50	680
0.75	3,330
1.10	57,600

Table 7. Reynolds number based on roughness height and local undisturbed conditions.

outlined an elliptical grid generation method for creating smooth orthogonal grids. The only necessary input is the grid point distribution along the two-dimensional sides of the three-dimensional domain. These distributions came from the equations in section III.C. The same values for S_ξ, S_η, S_ζ, and x_c as the shorter roughnesses were used. Figure 18 shows the grid in the vicinity of the $k/\delta = 1.10$ roughness element. All the grids use 600 points in the streamwise direction, 300 points in the wall normal direction, and 150 points in the spanwise direction. Only half of the domain was simulated in the z direction. Away from the roughness element, the grids used for each of the roughness elements match. The results were not confirmed to be grid converged.

The simulations for all the roughnesses reached a steady-state solution. Figure 19 shows density contours at the $z = 0$ symmetry plane for the four roughnesses. The $k/\delta = 1.10$ roughness clearly shows a shock generated slightly upstream of the roughness. Just downstream of the shock is an expansion fan which is followed by a weaker shock. The same structures are also visible in the shorter roughnesses but they become weaker as the roughness height decreases. The contours for the $k/\delta = 1.10$, 0.75, and 0.50 roughnesses show that the boundary layer has been significantly altered downstream of the roughness element. The boundary layer downstream of the $k/\delta = 0.25$ roughness element was not as greatly affected by the roughness.

Figure 20 shows a three-dimensional isosurface of the vorticity magnitude, $|\omega|$, for each roughness. The $|\omega|\delta/u_\infty = 1.5$ surface is shown. The main features for the $k/\delta = 1.10$ roughness is the horse-shoe vortex and the wake vortex. The horse-shoe vortex is the two outer streaks seen in the figure. It wraps around the front of the roughness element and then aligns itself with the flow direction downstream of the roughness element. The wake vortex is formed directly behind the roughness element. In the figure, it is the long streak located between the legs of the horse-shoe vortex. There is also a high vorticity region along the wall underneath the wake vortex. All the structures are straight and persist until the exit of the numerical domain. For the $k/\delta = 0.75$ roughness, the same structures are present but the legs of the horse-show vortex are smaller. For the $k/\delta = 0.50$ roughness, the horse-shoe vortex is no longer visible in the figure. The wake vortex and the high vorticity region near the wall are still present. For the $k/\delta = 0.25$ roughness, only a small portion of the wake vortex is visible.

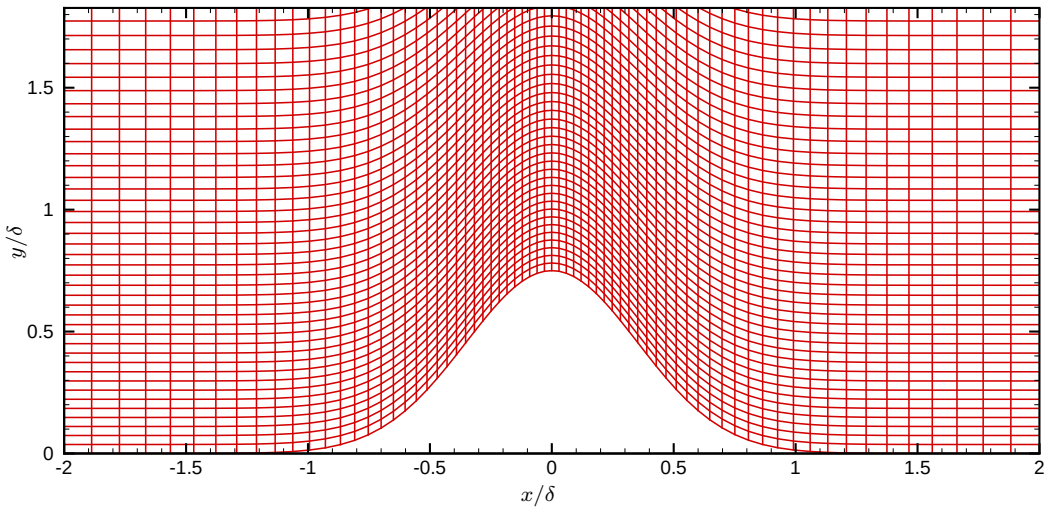

(a) $x - y$ plane at $z/\delta = 0$

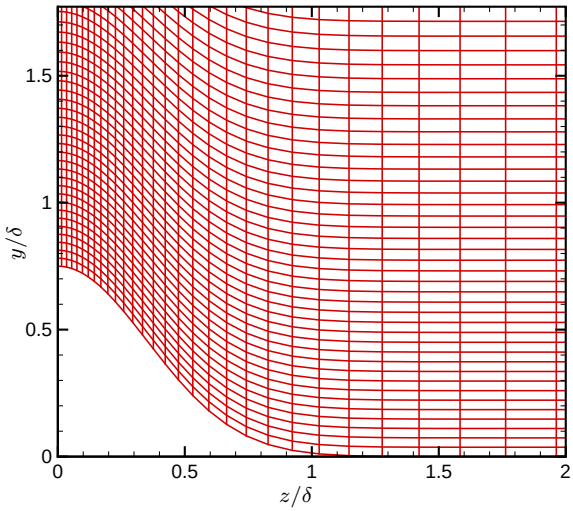

(b) $y - z$ plane at $x/\delta = 0$

Figure 17. Grid in the vicinity of the three-dimensional Gaussian roughness element with $k/\delta = 0.75$. Grid has 600 points in x direction, 300 points in y direction, and 150 points in z direction. Every fourth point shown in all directions.

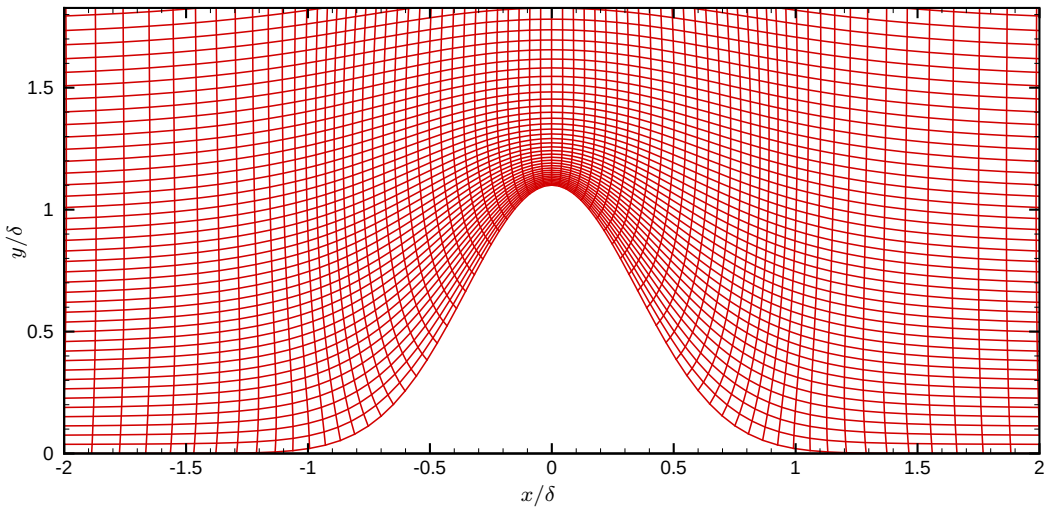

(a) $x - y$ plane at $z/\delta = 0$

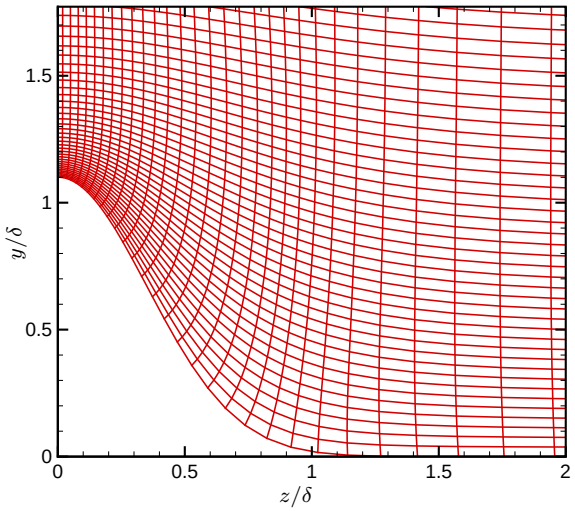

(b) $y - z$ plane at $x/\delta = 0$

Figure 18. Grid in the vicinity of the three-dimensional Gaussian roughness element with $k/\delta = 1.10$. Grid has 600 points in x direction, 300 points in y direction, and 150 points in z direction. Every fourth point shown in all directions.

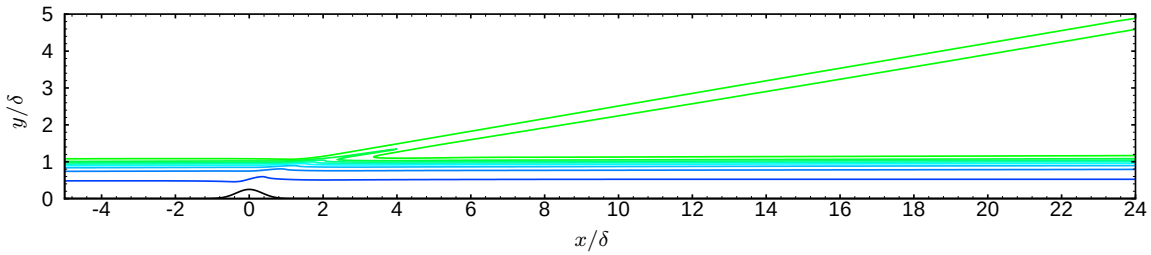

(a) $k/\delta = 0.25$

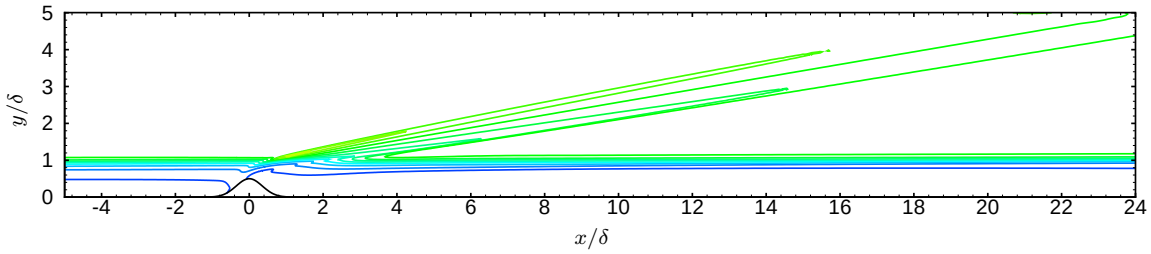

(b) $k/\delta = 0.50$

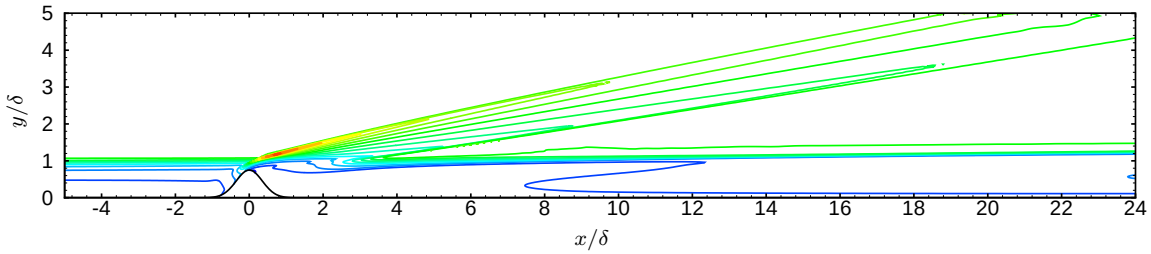

(c) $k/\delta = 0.75$

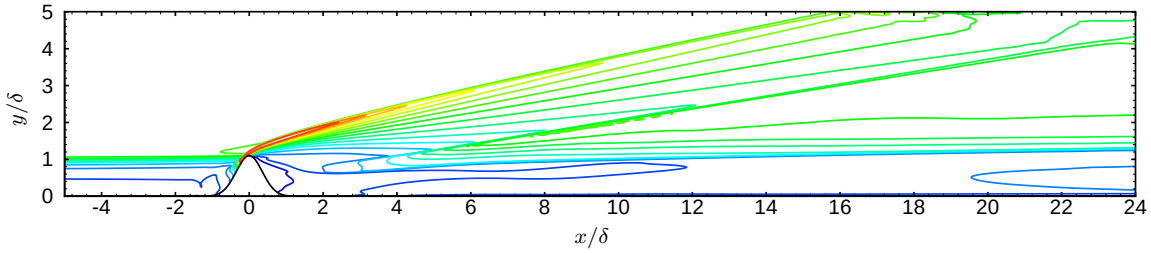

(d) $k/\delta = 1.10$

Figure 19. Density contours at $z = 0$ plane for Gaussian roughness elements. Non-dimensionalized as ρ/ρ_∞. 16 contour levels from 0.1 to 1.75.

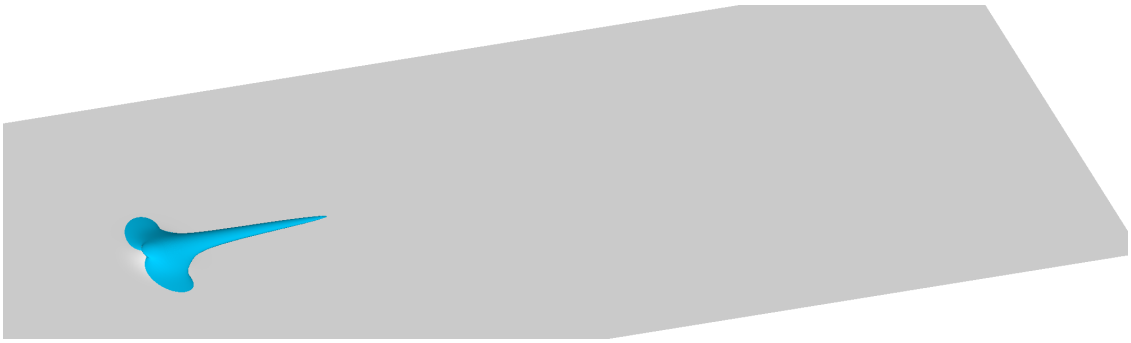

(a) $k/\delta = 0.25$

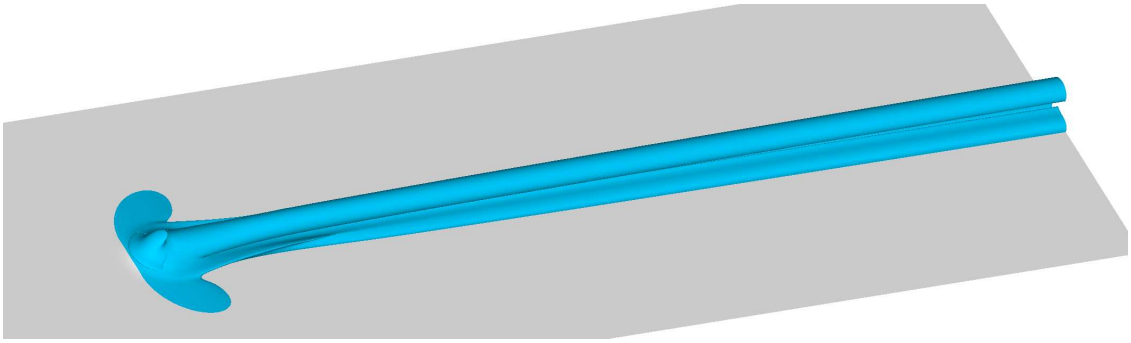

(b) $k/\delta = 0.50$

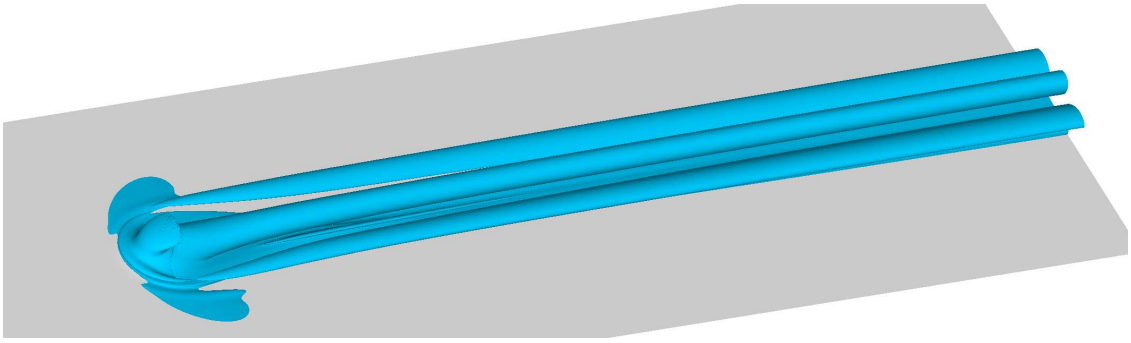

(c) $k/\delta = 0.75$

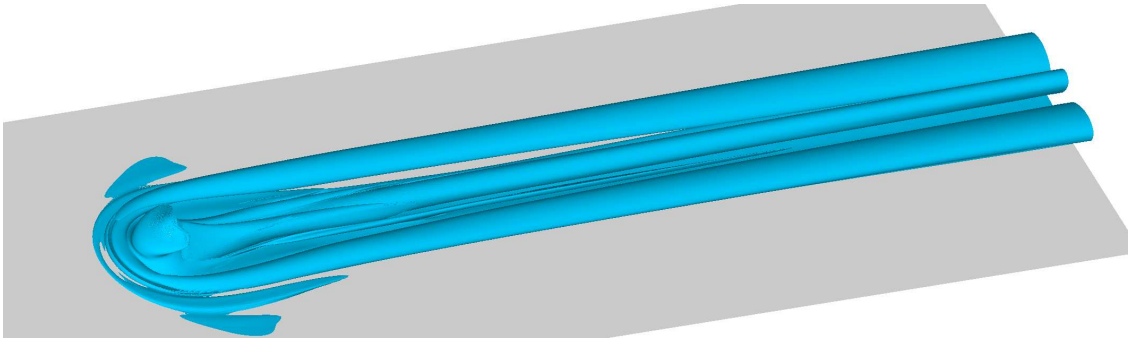

(d) $k/\delta = 1.10$

Figure 20. Vorticity magnitude isosurfaces for Gaussian roughness elements. Surface for $|\omega|\delta/u_\infty = 1.5$ shown. Flat plate shown in gray.

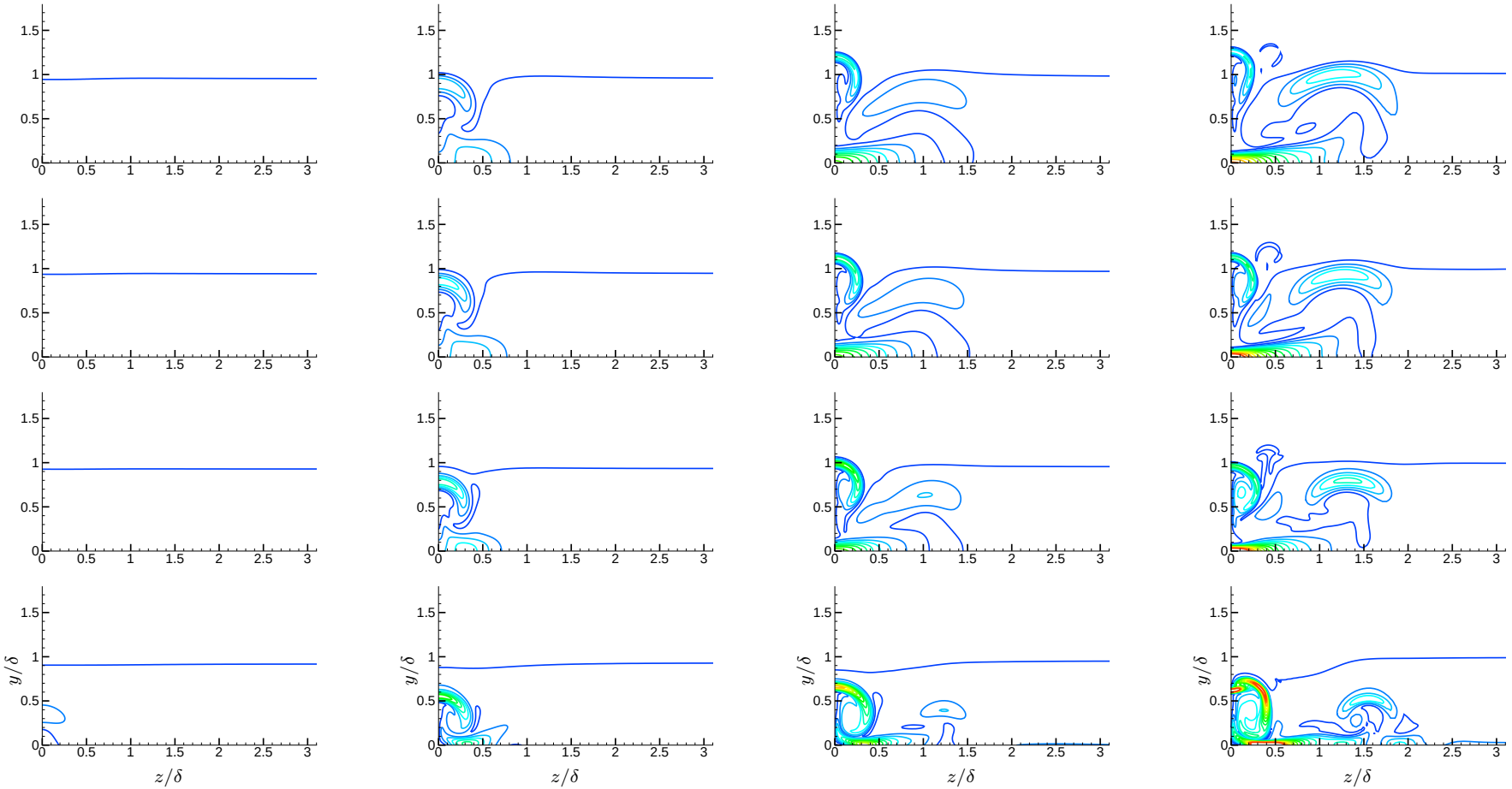

(a) $k/\delta = 0.25$ (b) $k/\delta = 0.50$ (c) $k/\delta = 0.75$ (d) $k/\delta = 1.10$

Figure 21. Vorticity magnitude contours at various x locations for Gaussian roughness elements. Non-dimensionalized as $|\omega|\delta/u_\infty$. 16 contour levels from 0 to 10. Starting from the bottom and moving vertically, the contours are at x/δ = 2, 9.3, 16.6, 23.9.

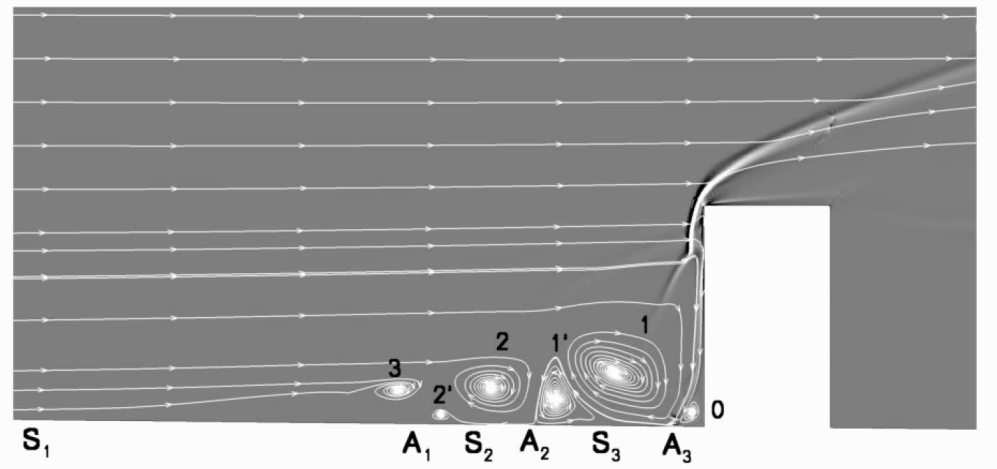

(a) Numerical shadowgraph contour with streamlines for Mach 6 flow over cylindrical roughness. From Bartkowicz et al.[18]

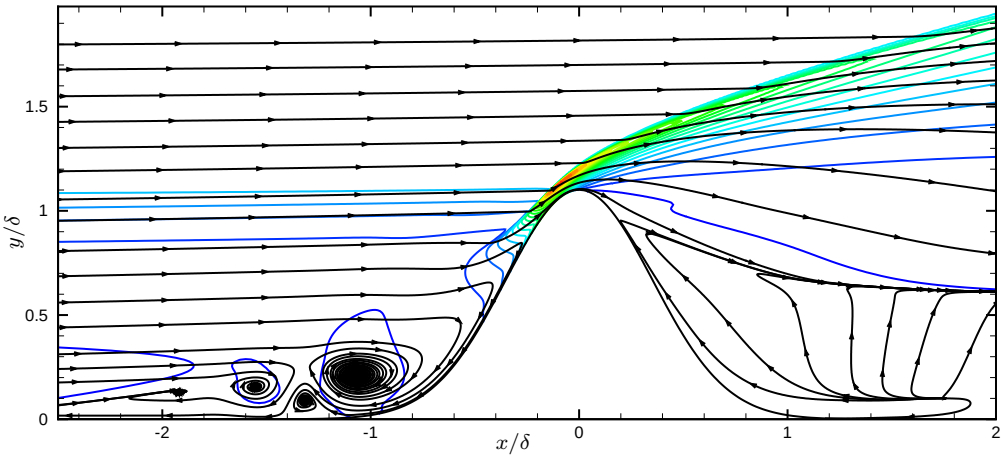

(b) Density contour with streamlines for Mach 6 flow over three-dimensional $k/\delta = 1.10$ Gaussian roughness. Density non-dimensionalized as ρ/ρ_∞. 21 contour levels from 0.2 to 4.2.

Figure 22. Streamlines for Mach 6 flow over cylindrical roughness and three-dimensional Gaussian roughness. Both plots are at the symmetry plane.

Figure 21 show contours of the magnitude of the vorticity vector at various x/δ locations for the four roughness elements. The contours for $k/\delta = 1.10$ show a large circular vortex in the center of the domain and a kidney-shaped vortex off to the side of the roughness. The circular vortex is the wake vortex while the kidney-shaped vortex is a leg of the horse-shoe vortex. Both vortices persist until the end of the numerical domain. At $x/\delta = 2$, the top of the wake vortex is at approximately $y/\delta = 0.8$ which is less then the height of the roughness. The vortex moves vertical as it progresses downstream. At $x/\delta = 24$, the top of the vortex has reach $y/\delta = 1.3$. The horse-shoe vortex also moves vertical as it progresses downstream but the increase is much less then the wake vortex. However, the size of the horse-shoe vortex increases greatly. The vortex approximately doubles in length within the numerical domain. The two vortices are also present in the contours for the $k/\delta = 0.75$ roughness but both are much weaker in magnitude. At $x/\delta = 2$, the top of the wake vortex is approximately the same height as the roughness element. The vortex also moves vertically like the wake vortex from the $k/\delta = 1.10$ roughness but the increase is less. The horse-shoe vortex also increase in length but to a greater extent then the $k/\delta = 1.10$ roughness. For the contour levels used in the figure, only the wake vortex is visible for the $k/\delta = 0.50$ roughness. The top of the wake vortex is higher then the roughness element at $x/\delta = 2$ with an approximate high of $y/\delta = 0.7$. The vortex moves vertically as it progresses downstream but appears to asymptote to approximately $y/\delta = 1.0$. For the $k/\delta = 0.25$ roughness, there is a very small wake vortex seen at $x/\delta = 2$ but it cannot be seen with these contour

levels anywhere downstream.

The 21 kHz instability of Wheaton and Schneider or any other unsteadiness was not seen in the simulations with a Gaussian roughness. This may have been due to the different roughness geometries. Bartkowicz et al.[18] where able to reproduce the instability measured by Wheaton and Schneider with numerical simulations of flow in the Purdue wind tunnel with a cylindrical roughness element. They found that the instability originates inside the vortex system located in front of the roughness near the wall. They postulate that the instability is being created by a jet of high momentum fluid which is created by the strong shock at the upper edge of the roughness and which flows down toward the vortex system. Figure 22 shows a comparison of the streamlines at the symmetry plane for the simulation of Bartkowicz et al. and the $k/\delta = 1.10$ simulation performed here. The Gaussian roughness appears to allow more fluid to flow over the roughness and thus weakens the jet which flows into the vortex system near the wall. The weakening of this jet may be the reason no instability was found in the current simulations.

V.C. Cylindrical Roughness

Simulations of flow over a flat plate with a cylindrical roughness are currently underway. Two roughness heights are being used: $k/\delta = 0.75$ and $k/\delta = 1.10$. The diameter of the roughness is 0.647δ for both simulations. The taller roughness has the same height and diameter as the roughness used by Wheaton and Schneider. The flow conditions match those provided by Wheaton and Schneider and are given in Table 6. The origin of the numerical domain is located at the center of the roughness element. The numerical domain starts 20δ upstream of the roughness and ends 25δ downstream of the roughness. The domain has a height of 5δ and half width of 7.5δ. The Re_k match the values from the three-dimensional Gaussian and are listed in Table 7. The simulation for the $k/\delta = 1.10$ roughness has only just begun so no results will be presented here.

The grids being used were generated algebraically using the equations from section III.C. Figure 23 shows the grid in the vicinity of the $k/\delta = 0.75$ roughness. The $k/\delta = 0.75$ grid has 800 points in the x direction, 600 points in the y direction, and 600 points in the z direction. The grid was generated with $S_\xi = 10.44$, $S_\eta = 6.8$, $S_\zeta = 3.96$, $x_c = -0.375\delta$, $y_c = 1.5\delta$, $L = 0.2994$, and $P = 15$. Both sides of the domain in the the z direction are being simulated.

The results for the $k/\delta = 0.75$ roughness being presented here are only preliminary. The simulation has not reached a steady-state or periodic solution yet. Figure 24 shows density contours at the $z = 0$ symmetry plane for the current state of the the simulation. The large structures seen downstream of the roughness elements are just the initial transients created by the simulation's initial condition. Although the entire flow field is still undergoing transient changes, the flow in the immediate vicinity of the roughness is no longer displaying large changes with time. Figure 25 shows the streamlines near the $k/\delta = 0.75$ roughness in the $z/\delta = 0$ plane and the $x - z$ plane one grid point away from the wall. The streamlines show the creation of a vortex system generated upstream of the roughness which is similar to the results of Bartkowicz et al.[18]

VI. Conclusion

Results from numerical simulations of hypersonic flow over isolated roughness elements were presented. Most of the simulations utilized a third-order cut-cell method combined with a fifth-order WENO which results in a globally fourth-order scheme. Two-dimensional and three-dimensional test cases show excellent agreement to results obtained from a body-fitted grid simulation. Preliminary results from Mach 6 flow over $k/\delta = 0.75$ cylindrical roughness was also presented and a simulation with a $k/\delta = 1.10$ roughness is currently underway. In addition, the results from simulations of Mach 6 flow over three-dimensional Gaussian roughnesses of varying heights computed with body-fitted grids were also reported.

Acknowledgments

The authors gratefully acknowledge support by the NASA Fundamental Aeronautics Program, under cooperative agreement NNX07AC39A, monitored by Dr. Meelan Choudhari and the partial support of the AFOSR/NASA National Center for Hypersonic Research in Laminar-Turbulent Transition. The authors thank the NASA Advanced Supercomputing Division and TeraGrid for providing computer time to run the numerical simulations.

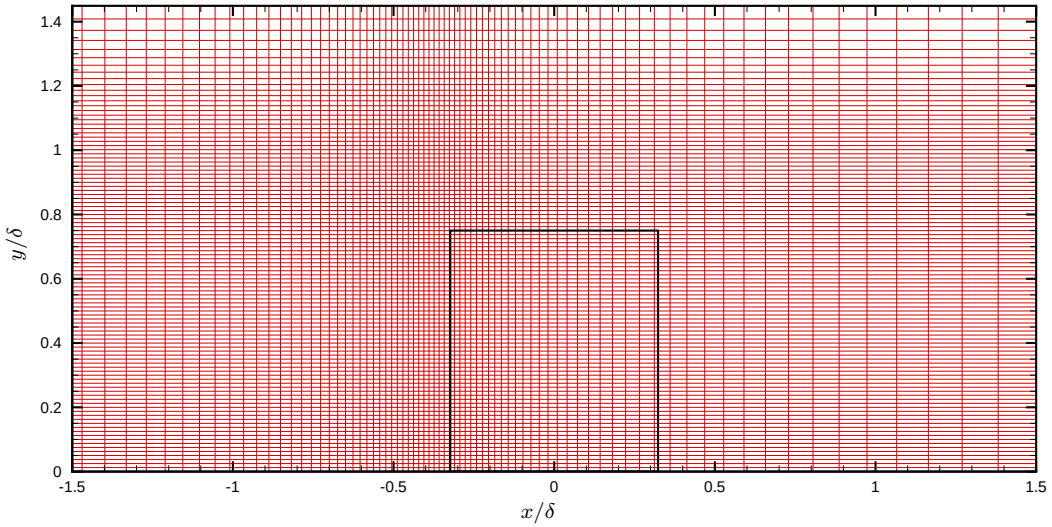

(a) $x - y$ plane

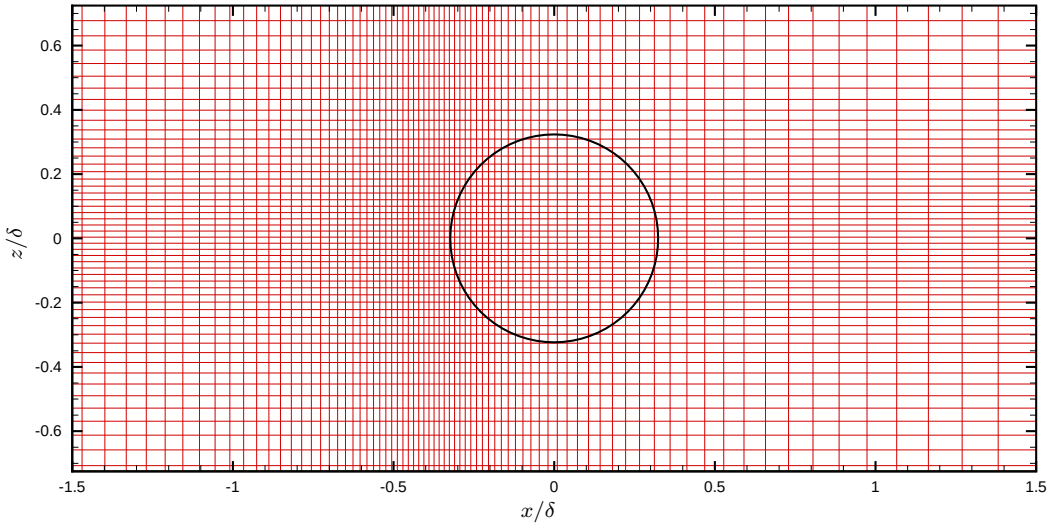

(b) $x - z$ plane

Figure 23. Grid in the vicinity of the three-dimensional cylindrical roughness element with $k/\delta = 0.75$. Roughness element shown in black. Grid has 800 points in x direction, 600 points in y direction, and 600 points in z direction. Every fifth point shown in all directions.

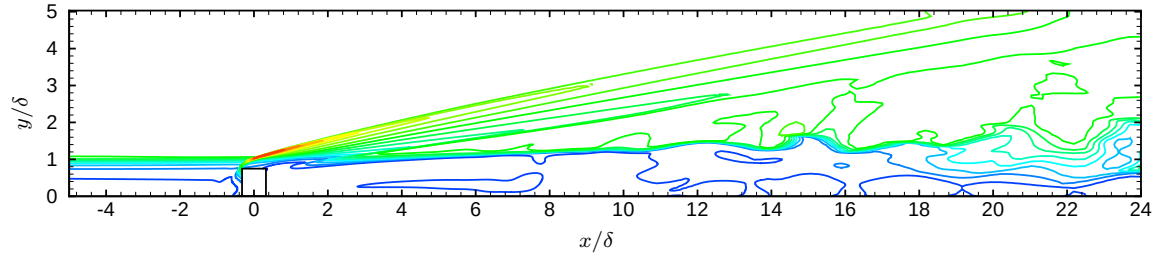

Figure 24. Density contours at $z = 0$ plane for $k/\delta = 0.75$ cylindrical roughness. Non-dimensionalized as ρ/ρ_∞. 16 contour levels from 0.1 to 1.75.

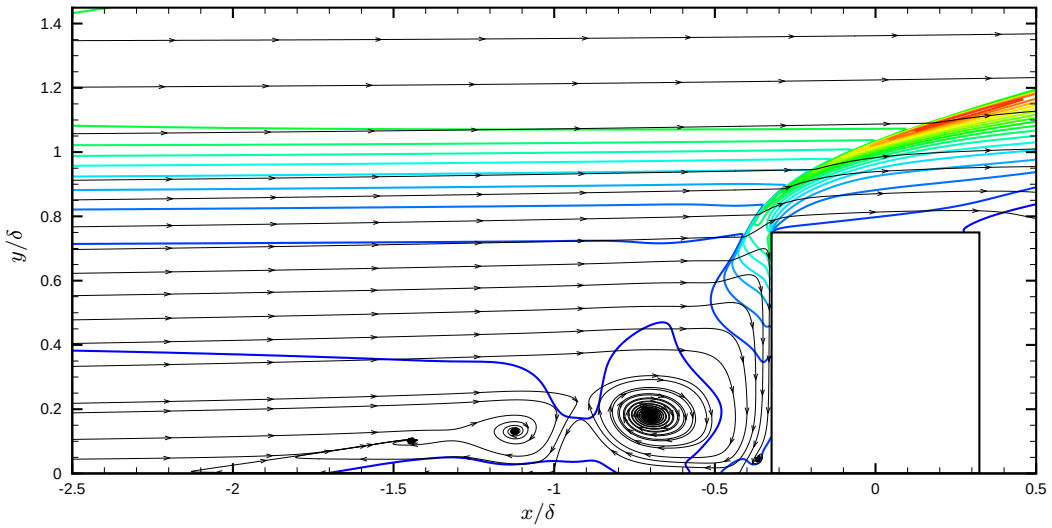

(a) Streamlines and density contour at $z/\delta = 0$. Density non-dimensionalized as ρ/ρ_∞ with 18 levels from 0.2 to 1.9.

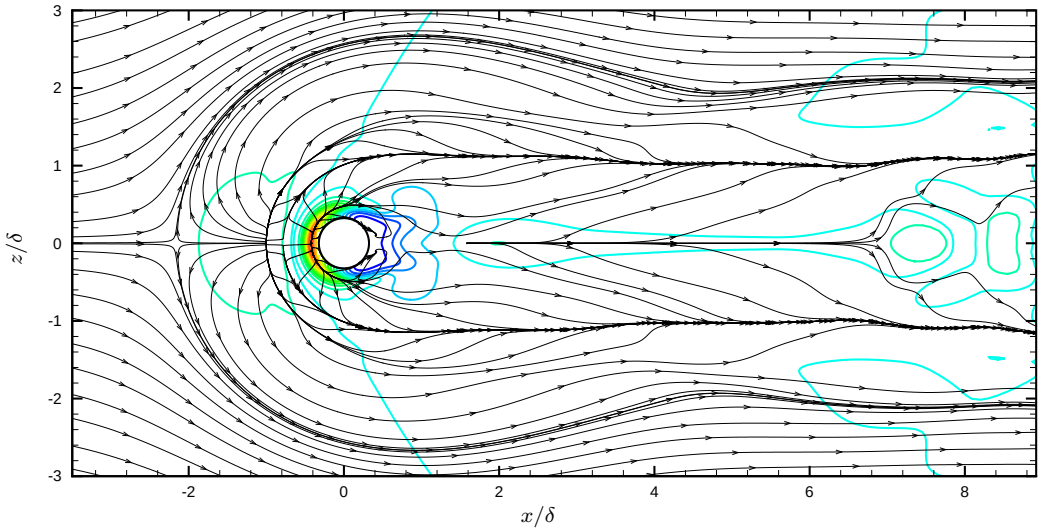

(b) Streamlines and pressure contour one grid point away from wall. Pressure non-dimensionalized as p/p_∞ with 15 levels from 0.6 to 2.0.

Figure 25. Streamlines for $k/\delta = 0.75$ cylindrical roughness

References

[1]Berry, S. and Horvath, T., "Discrete Roughness Transition for Hypersonic Flight Vehicles," AIAA Paper 2007-307, Jan 2007.

[2]Schneider, S. P., "Effects of Roughness on Hypersonic Boundary-Layer Transition," *Journal of Spacecraft and Rockets*, Vol. 45, No. 2, Mar-Apr 2008, pp. 193–209.

[3]Tumin, A. and Reshotko, E., "Spatial theory of optimal disturbances in boundary layers," *Physics of Fluids*, Vol. 13, No. 7, July 2001, pp. 2097–2104.

[4]White, E. and Reshotko, E., "Roughness-Induced Transient Growth in a Flat-Plate Boundary Layer," AIAA Paper 2002-0138, Jan 2002.

[5]White, E. and Ergin, F., "Receptivity and Transient Growth of Roughness-Induced Disturbances," AIAA Paper 2003-4243, June 2003.

[6]White, E. B., Rice, J. M., and Gokhan Ergin, F., "Receptivity of stationary transient disturbances to surface roughness," *Physics of Fluids*, Vol. 17, No. 6, June 2005, pp. 064109.

[7]Fischer, P. and Choudhari, M., "Numerical simulation of roughness-induced transient growth in a laminar boundary layer," AIAA Paper 2004-2539, June 2004.

[8]Choudhari, M. and Fischer, P., "Roughness-Induced Transient Growth," AIAA Paper 2005-4765, June 2005.

[9]Reshotko, E. and Tumin, A., "Role of transient growth in roughness-induced transition," *AIAA Journal*, Vol. 42, No. 4, Apr 2004, pp. 766–770.

[10]Reda, D. C., "Correlation of Nosetip Boundary-Layer-Transition Data Measured In Ballistics-Range Experiments," *AIAA Journal*, Vol. 19, No. 3, 1981, pp. 329–339.

[11]Reda, D. C., "Review and Synthesis of Roughness-Dominated Transition Correlations For Reentry Applications," *Journal of Spacecraft And Rockets*, Vol. 39, No. 2, Mar 2002, pp. 161–167.

[12]Acarlar, M. and Smith, C., "A Study of Hairpin Vortices in a Laminar Boundary Layer . Part 1. Hairpin Vortices Generated by a Hemisphere Protuberance," *Journal of Fluid Mechanics*, Vol. 175, Feb 1987, pp. 1–41.

[13]Ergin, F. G. and White, E. B., "Unsteady and Transitional Flows Behind Roughness Elements," *AIAA Journal*, Vol. 44, No. 11, Nov 2006, pp. 2504–2514.

[14]Chang, C.-L. and Choudhari, M., "Hypersonic Viscous Flow over Large Roughness Elements," AIAA Paper 2009-0173, 2009.

[15]Papamoschou, D. and Roshko, A., "The Compressible Turbulent Shear-Layer: An Experimental Study," *Journal of Fluid Mechanics*, Vol. 197, Dec 1988, pp. 453–477.

[16]Danehy, P., Bathel, B., Ivey, C., Inman, J., and Jones, S., "NO PLIF Study of Hypersonic Transition Over a Discrete Hemispherical Roughness Element," AIAA Paper 2009-394, Jan 2009.

[17]Chang, C.-L., Choudhari, M., and Li, F., "Numerical Computations of Hypersonic Boundary-Layer over Surface Irregularities," AIAA Paper 2010-1572, Jan 2010.

[18]Bartkowicz, M. D., Subbareddy, P., and Candler, G., "Numerical Simulations of Roughness Induced Instabillity in the Purdue Mach 6 Wind Tunnel," AIAA Paper 2010-4723, 2010.

[19]Wheaton, B. M. and Schneider, S. P., "Roughness-Induced Instabillity in a Laminar Boundary Layer at Mach 6," AIAA Paper 2010-1574, 2010.

[20]Ward, C., Wheaton, B., Chou, A., Gilbert, P., Steen, L., and Schneider, S., "Boundary-Layer Transition Measurements in a Mach-6 Quiet Tunnel," AIAA Paper 2010-4721, 2010.

[21]Schneider, S. P., "Fabrication and testing of the Purdue Mach-6 quiet-flow Ludwieg tube," AIAA Paper 2000-0295, Jan 2000.

[22]Jiang, G. and Shu, C., "Efficient Implementation of Weighted ENO Schemes," *J. Comput. Phys.*, Vol. 126, No. 1, 1996, pp. 202–228.

[23]Duan, L., Wang, X., and Zhong, X., "A high-order cut-cell method for numerical simulation of hypersonic boundary-layer instability with surface roughness," *Journal of Computational Physics*, Vol. 229, No. 19, 2010, pp. 7207 – 7237.

[24]Zhong, X. L., "High-order finite-difference schemes for numerical simulation of hypersonic boundary-layer transition," *Journal of Computational Physics*, Vol. 144, No. 2, Aug 1998, pp. 662–709.

[25]Marxen, O. and Iaccarino, G., "Numerical Simulation of the Effect of a Roughness Element on High-Speed Boundary-Layer Instabillity," AIAA Paper 2008-4400, June 2008.

[26]Xu, S. and Martin, M., "Assessment of inflow boundary conditions for compressible turbulent boundary layers," *Physics of Fluids*, Vol. 16, No. 7, July 2004, pp. 2623–2639.

[27]Schneider, S. P., Rufer, L., and Skoch, C., "Shakedown of the Purdue Mach-6 Quiet-Flow Ludwieg Tube," AIAA Paper 2001-0457, Jan 2001.

[28]Marxen, O. and Iaccarino, G., "An Immersed Boundary Method for Numerical Simulations of Boundary Layers with Roughness," *Center for Turbulence Research Annual Research Briefs*, 2008.

[29]Spekreijse, S. P., "Elliptic Grid Generation Based On Laplace Equations And Algebraic Transformations," *Journal of Computational Physics*, Vol. 118, No. 1, Apr 1995, pp. 38–61.